

**CZECH TECHNICAL UNIVERSITY
IN PRAGUE**

Faculty of Nuclear Sciences and Physical Engineering

Department of Physics



**Interpretation of the parameters of cosmic air showers
using current models of the nucleus-nucleus
interactions.**

Diploma thesis

Michal Nyklíček

Supervisor: Jan Řídký, CSc., Institute of Physics, Academy of Sciences
of the Czech Republic, v.v.i. Prague

Consultant: Mgr. Petr Trávníček PhD., Institute of Physics, Academy
of Sciences of the Czech Republic, v.v.i. Prague

Academic year 2007/2008

Prohlašuji, že jsem svou diplomovou práci vypracoval samostatně a použil jsem pouze podklady (literaturu, projekty, SW atd.) uvedené v příloženém seznamu.

Nemám závažný důvod proti užití tohoto školního díla ve smyslu §60 Zákona č.121/2000 Sb., o právu autorském, o právech souvisejících s právem autorským a o změně některých zákonů (autorský zákon).

V praze, 20.4.2008

Michal Nyklíček

Acknowledgements

First of all, I would like to thank to the supervisor of this work, Jan Řídký that he led this work. Although he is very busy he gave me many useful suggestions. I thank him also excellent consultations and also I have to thank him for the corrections of the text.

My thanks go to Petr Trávníček, who was consultant of this work. He gave me many valuable technical advices. I have to thank Petr for his enormous support, for plenty of time, which he has spend with me and for useful discussions. And I have to thank him for the text corrections, too.

I would like to thank to the members of the Prague part of the Czech group of the Pierre Auger Collaboration for interesting discussions.

I have also to thank to my colleague Karel Smolek for his advices and mainly for his support during my obtaining of the skills at C++ and ROOT.

My thanks also go to my mother and to my girlfriend for their support during my studies and for their patience with me.

Interpretace parametrů atmosferických spršek kosmického záření pomocí současných modelů jádro-jaderných interakcí

Michal Nyklíček

Abstrakt

Stanovení chemického složení kosmického záření z dat fluorescenčních detektorů se značně opírá o naši znalost jádro-jaderných interakcí odehrávajících se ve vznikajících sprškách. Oproti tomu stanovení energie spršky z jejího fluorescenčního profilu v atmosféře je modelově méně závislé. Modely se nicméně používají pro odhad chybějící energie nesené neutrinu a miony, o kterou se kalorimetrické měření fluorescenčních detektorů opravuje. Cílem práce je porovnat mezi sebou modely jádro-jaderných interakcí, které se v současné době používají pro popis spršky kosmického záření a stanovit jejich vliv na interpretaci dat v případě určování chemického složení kosmického záření a energie rekonstruované fluorescenčními detektory.

Klíčová slova: kosmické záření, jaderné interakce, chemické složení kosmického záření, chybějící energie

Interpretation of the parameters of cosmic air showers using current models of the nucleus-nucleus interactions.

Michal Nyklíček

Abstract

The determination of the chemical composition of cosmic rays from data measured by fluorescence detectors is strongly dependent on our knowledge on nucleus-nucleus interactions which occur in showers. On the other hand, the reconstruction of shower energy from its fluorescence profile in atmosphere is less model dependent. Nevertheless, models are used for estimation of missing energy carried out by neutrinos and by muons. Missing energy is then used for corrections of the calorimetric energy measured by fluorescence detectors. The goal of this work is to compare these models of nucleus-nucleus interactions, which are presently used for description of cosmic ray showers and estimate their influence to data interpretation in the case of the chemical composition of cosmic rays and energy, reconstructed in fluorescence detectors.

Keywords: cosmic rays, hadronic interactions, chemical composition of cosmic rays, missing energy

Contents

1	Introduction	9
2	History	11
3	Primary Cosmic Rays	14
3.1	Composition	14
3.2	Energy spectra	16
3.3	Propagation	18
3.4	Anisotropy	19
3.5	Origin of cosmic rays	20
3.5.1	Bottom-up models	20
3.5.2	Top-down models	23
3.6	Acceleration mechanism	24
3.6.1	Fermi's original theory	24
3.6.2	First order Fermi acceleration	26
3.6.3	Spectral index	27
3.6.4	Direct acceleration	28
3.6.5	Hillas condition	28
3.7	Galactic and extragalactic cosmic ray	29
3.7.1	Galactic cosmic ray	29
3.7.2	Extragalactic cosmic ray	30
3.7.3	Transition from galactic to extragalactic	30
3.8	GZK cut-off	30
4	Secondary Cosmic Rays	34
4.1	Basic description and features	34
4.2	Toy model	36
4.3	The shower components	37
4.4	The development of the shower	38
4.4.1	Ionization energy loss	38
4.4.2	Particle decays	38
4.4.3	Particle interactions	40
4.4.4	Čerenkov radiation	40
4.4.5	Atmospheric fluorescence	41

4.4.6	The longitudinal development of the shower	42
4.4.7	The lateral profile	43
5	The Measurement Techniques of UHECR	45
5.1	The Pierre Auger Observatory	45
5.1.1	The surface detectors	47
5.1.2	The fluorescence detectors	48
6	The Simulation Programs and Models	50
6.1	The simulations programs	50
6.1.1	CORSIKA	50
6.1.2	CONEX	51
6.1.3	SENECA	51
6.2	The interactions models	52
7	The Determination of the Chemical Composition	58
7.1	The elongation rate	58
7.2	Two component model	58
7.3	Mean logarithmic mass	59
8	Results of Simulation in the SENECA Simulation Code	60
8.1	Results of simulation of X_{max}	60
8.2	The data measured by the Pierre Auger Observatory	66
8.3	The influence of high energy interaction models to the determination of chemical composition of cosmic rays	67
8.3.1	Results from individual models	67
8.3.2	Model dependence	70
9	The Missing Energy	78
9.1	The computation of the missing energy	78
9.2	The results of computation of the missing energy	79
10	Summary and Conclusions	88
11	References	90

Chapter 1

Introduction

The Cosmic Rays (CRs) are energetic particles, originated from the Universe and they are hitting Earth's atmosphere at every moment. Most of these particles are protons and smaller fractions are alpha particles, heavier nuclei, electrons, positrons and photons.

The energy range of CRs is very wide, it extends 12 orders of magnitude. The highest energies of CR reach hundreds of EeV (about 20 joules - a macroscopic energy). For comparison, current accelerators can accelerate particles "only" to energies tens of TeV, 7 orders of magnitude lower. The study of CRs presents a unique possibility to study high energy processes in the sources as well as high energy interactions of CRs with atmospheric nuclei. The CRs with the highest energies represent "a new window of astronomy": they can give us information about their sources, features of interstellar space and magnetic fields.

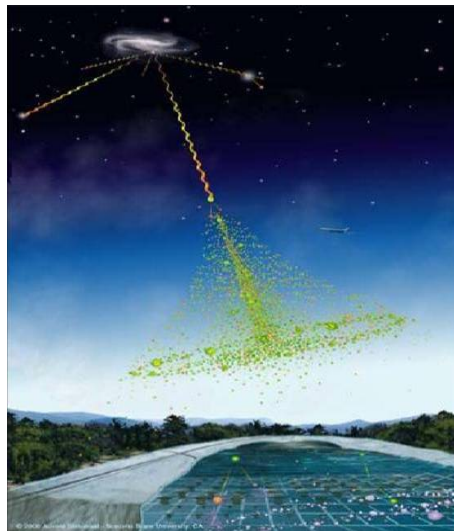


Figure 1.1: The propagation of CR from its source to the ground on the Earth.

At the present, there are four basic questions on CR:

- How are the particles accelerated to such high energies?
- Where do they come from? In which objects are they accelerated?
- How do they propagate through the interstellar space?
- Where the spectrum stops?

We can distinguish two kinds of CR - primary cosmic rays and secondary cosmic rays. If some particle is accelerated at its source and then the particle propagates through the Universe - this is called **primary cosmic ray**. If this particle hits the Earth's atmosphere and creates a cascade of secondary particles - the products are called **secondary cosmic rays**.

The main goals of this work are to simulate cosmic ray showers with SENECA and CONEX, to determine the influence of the high-energy interaction models on the estimation of the chemical composition, to determine the missing energy and also to show the influence of high-energy interaction models on the missing energy estimation.

Chapter content

In the second chapter of this work the development of the field of CR is explained on examples of important discoveries.

The third chapter deals with primary CR. The main features of primary CR are described - chemical composition of CR, the energy spectrum, origin of CR, how the CR particles can reach their energies and how they are propagated through the Universe.

The fourth chapter describes secondary CR, physics of atmospheric, showers behavior of different shower components.

The measurement techniques of ultra-high energy cosmic rays are mentioned in the fifth chapter. The different measurement techniques are described on the example of Pierre Auger Observatory.

The present programs, which are used for simulations of the showers of CRs are mentioned in the sixth chapter. Also the the interactions models are referred to.

Some models, how can be the chemical composition of the primary CR particle determined from the combination of simulated data and data from measurement are described in the seventh chapter.

The results of simulation in SENECA simulation code are shown. The simulations of the maximum of the shower are compared for different interaction models. Also the influence of the interaction models to the chemical composition of CRs is discussed in the eighth chapter.

The missing energy which was calculated from the data obtained from the simulations with CONEX is described in the ninth chapter.

The tenth chapter summarize briefly the studied problematics.

Chapter 2

History

At the beginning of the 19th century, French physicist **Henri Becquerel** discovered that certain elements are unstable, and they transmute into other elements and in some processes emit what appeared to be particles. These "particles" were given the name "radiation", and the process itself was referred to as "radioactive decay".

It was noticed that an instrument called "electroscope" (see fig.2.1) would spontaneously discharge in the presence of radioactive materials. The rate of discharge of an electroscope was then used as a measure of the level of radiation. The electroscope thus became a standard instrument for studying radiation and radioactive materials in the first decades of the 20th century.

However, physicists noticed that electroscopes were found to discharge slowly even in the absence of radioactive matter. This residual discharge could not be attributed to leakage. It seemed to be due to a background radiation.

The first attempt to study background radiation was made in the experiment by **Theodor Wulf**. The chamber was placed on the top of the Eifel tower. The results surprisingly showed, that the ionization decrease compared to Earth surface was not as large as expected.

To study the source of this background, Austrian physicist **Victor. F. Hess** (see fig. 2.2) made measurements of radiation levels at different altitudes with electroscopes aboard a balloon⁽¹⁾. The motivation for this study was to distance the electroscopes from radiation sources in the Earth. Surprisingly, he found that the radiation levels increased with altitude⁽²⁾. Hess interpreted this result as a consequence of radiation entering the atmosphere from outer space. He gave this phenomenon the name "Cosmic Radiation", which later evolved to "Cosmic Rays". Hess was awarded the Nobel Prize in 1936 for his discovery.

After the discovery of CRs, there were many questions: What is CR? Which qualities does it have?

In the year 1925, **Andrews Millikan** made a suggestion, that CRs are a result of forming nuclei from protons and electrons. In the twenties, there was a suggestion,

¹The actual discovery flight was made from Usti nad Labem in northern Bohemia.

²The discharging of the electroscope was 9 times faster.



Figure 2.3: Pierre Auger.

At the beginning of the 1960s, the relict microwave radiation was discovered⁽³⁾. And in the year 1966 **K. Greisen** and independently **V. Kuzmin** with **G. Zatsepin** predicted, that CR particles interact with photons of relict radiation and due to this interactions they loose energy. They also calculated the threshold energy of CR particles, which depends at its initial energy. This threshold energy is called **GZK cutoff**.

The first extremely high-energy particle was registered in 1962 by experiment Volcano Ranch Array in New Mexico. This particle had energy of about 10^{20} eV. The most energetic particle detected so far was measured by the experiment Fly's Eye (USA). It detected a particle with primary energy 3.2×10^{20} eV (15.10.1991).

In the year 2001 the construction of 3000 km^2 array - so far the largest CR experiment - started. Its name - "Pierre Auger Observatory" - reminds the roots of this scientific field.

³By A.Penzias and R. Wilson.

Chapter 3

Primary Cosmic Rays

Primary cosmic rays are particles, which were somewhere created and accelerated, they propagate through the Universe until they interact with the Earth's atmosphere. The basic description of primary CRs will be now given⁽¹⁾.

3.1 Composition

All known stable particles are abundant in CRs. There are particles like protons, alpha particles, heavier nuclei, positrons, electrons and photons. Particle composition of CR depends on the energy.

The particle composition of primary CRs in the energy region⁽²⁾ of about 10 GeV is approximately 90% protons, 7% alpha particles, 1% atomic nuclei, 1% electrons and positrons and small fraction of gammas. In the energy region of about TeV to PeV, there is different composition. About 50% protons, 25% alpha particles, 13% CNO nuclei (carbon, nitrogen, oxygen) and 13% are nuclei with atomic number closer to Fe [1].

The Earth surface is hit by particles which were created within our Solar system and by particles which were created outside our Solar system (cosmic rays). The relative abundances of cosmic rays are compared with abundances of elements in the solar system (see fig. 3.1). The symbols in fig. 3.1 have the following meaning: Solid circles: low energy data, 70 - 280 MeV/A; open circles: high energy data, 1000 - 2000 MeV/A. Solar system abundances are shown by open diamonds. Both solar system and cosmic ray abundances show the odd even effect, even Z nuclei being more abundant. There is, however, striking difference between the two compositions [2]. The difference is between the abundances of the two groups of elements: Li, Be, B and Sc, Ti, V, Cr, Mn. This difference is well understood and is an important tool for understanding the propagation and confinement of CRs in the Galaxy. These two groups of elements are absent as end products of stellar nucleosynthesis. But they are products of spallation of the abundant nuclei of carbon and oxygen (Li, Be, B) and of iron (Sc, Ti, V, Cr,

¹The dominant sources of literature are: [2], [4], [1] and [5].

²In this region is composition of primary CR measured directly.

Mn). This suggests that they are produced by collisions of CRs in the interstellar medium (ISM). From the knowledge of the cross section of spallation, one can learn something about the amount of the matter traversed by CRs between production and observation. (Secondary particles, such as photons, neutrinos and antiprotons should be also produced in CR interactions with ISM.) For CRs in the GeV energy range the mean amount of matter traversed is of order $X = 5 \sim 10 \text{ g/cm}^2$. The density ρ_N in the disk of the Galaxy is of the order of one proton per cm^3 , so this thickness of material corresponds to the distance of:

$$l = \frac{X}{m_p \rho_N} = 3 \times 10^{24} \text{ cm} \approx 1000 \text{ kpc}.$$

Because CRs may spend some time in the more diffuse galactic halo, this is a lower limit to the distance travelled. [2]

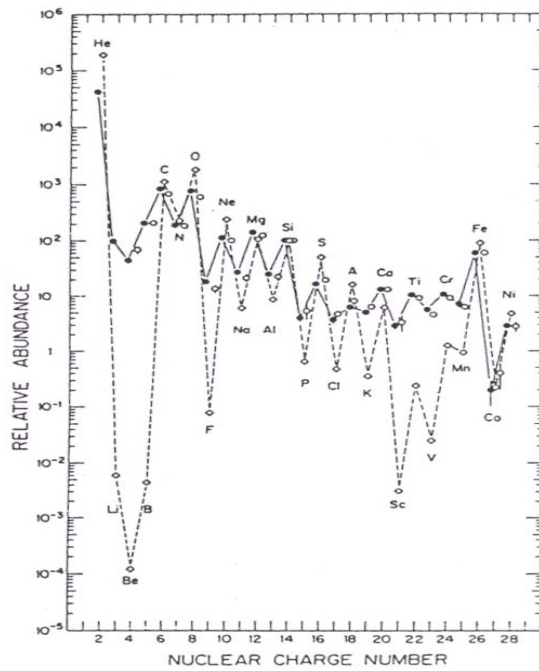


Figure 3.1: The cosmic ray elemental abundances (He-Ni) measured at Earth compared to the solar system abundances [2]. Solid circles: low energy data, 70 - 280 MeV/A; open circles: high energy data, 1000 - 2000 MeV/A. Solar system abundances are shown by open diamonds. Solid line represents CRs elements and dashed line represent solar system elements.

3.2 Energy spectra

The energy of CR starts approximately at about GeV and continues up to hundreds of EeV. The flux at lower limit is influenced by solar activities. The charged moving particles from the Sun, so-called solar wind, form a magnetic field, which hinders the low energetic CR particles to reach our solar system. The intensity of solar wind varies with solar cycle and the CR flux as measured at the Earth is inversely correlated to solar activity.

The energy spectrum of CRs is the dependence of the flux of CRs particles on the energy.

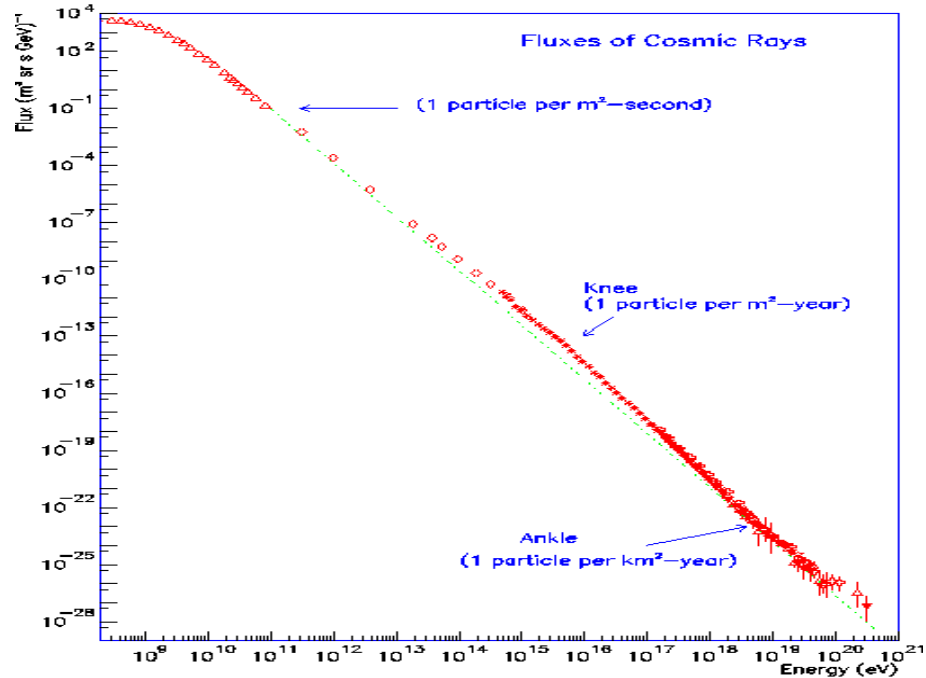


Figure 3.2: All particle energy spectra.

Differential energy spectrum (see fig. 3.2) can be approximated by inverse power law equation:

$$\frac{dN}{dE} \approx E^{-\alpha}, \quad (3.1)$$

where E is the energy of CR particle, N is a number of particles and α is a spectral index of the exponential decrease of the number of the particles with the energy.

As can be seen in the fig. (3.2) and more clearly in (3.3), the slope of differential energy spectrum is not constant. In the energy range 10^{10} eV to 10^{15} eV the value of α is equal approximately to 2.7. Above this range of energy, the slope of differential energy spectrum is more steeper. This changing point in slope of the spectrum is called

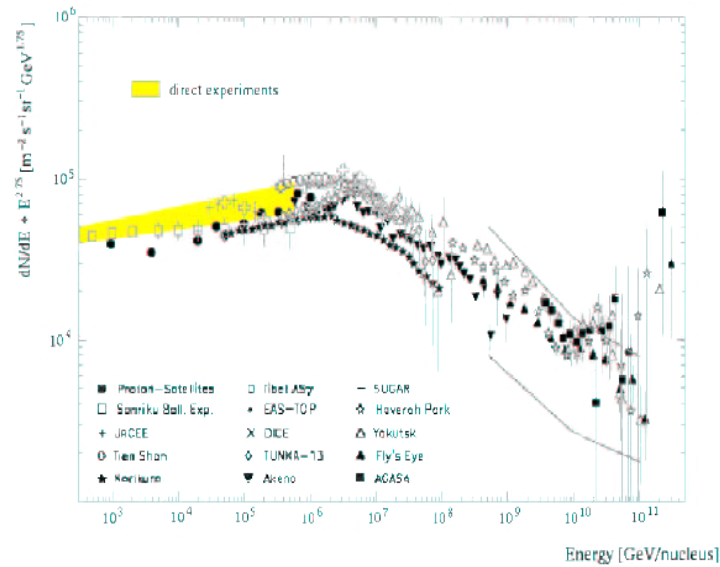


Figure 3.3: The energy spectrum of CR multiply 2.7. This spectrum is result of many different experiments. This picture was taken from [3].

the "knee". The steepest slope of spectrum is in the energy range between 10^{15} eV to 10^{18} eV. In this part of spectrum, the α value is approximately 3.0. The next change of the spectrum slope is in the energy region around 4×10^{18} eV. This point is called the "ankle". In the energy region between 10^{19} eV to 5×10^{19} eV the α value is again 2.7. Beyond the energy value 5×10^{19} eV the steepest slope of spectrum is expected due to the GZK effect. Some experiments confirm this expectation (HIRES⁽³⁾) and some experiments rejected this expectation (AGASA⁽⁴⁾). It is supposed, that recently built Pierre Auger Observatory⁽⁵⁾ will give final answer about this energy region.

If we look at single element spectra and compare them, we can notice an interesting feature - secondary nuclei (i.e. those produced as spallation products of abundant species) have significantly steeper spectra than the primary nuclei. The secondary to primary ratios decrease as energy increases. This tells us that the higher energy cosmic ray diffuse out of the galaxy faster [2].

In the fig. (3.4) one can see the difference in the energy spectra between some elements in CR. For energies to the left of the vertical line the flux varies significantly during the solar cycle (an effect called "solar modulation" [2].)

³High Resolution Fly's Eye, Utah, USA. This experiment uses fluorescence detectors.

⁴Akeno Giant Air Shower Array, Tokyo, Japan. This experiment used scintillation counters and muon counters.

⁵It will be described in chapter 5.

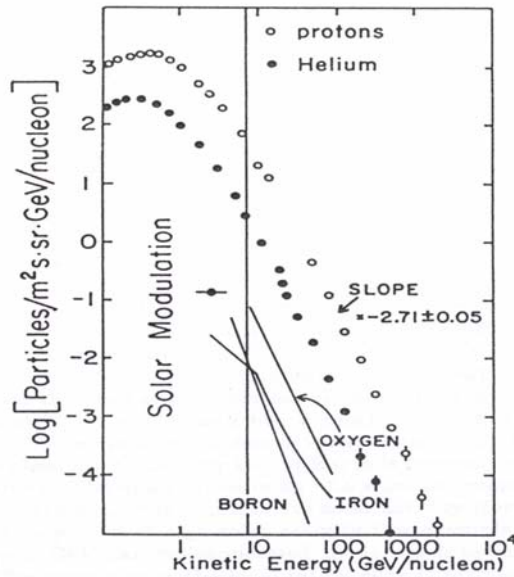


Figure 3.4: Energy spectra of several components of the cosmic rays. [2]

3.3 Propagation

As it was already mentioned above, in CRs there is much greater proportion of "secondary" nuclei, such as Li, Be, B, than it is generally found in the universe. These nuclei are almost absent as end products of stellar nucleosynthesis. They are spallation products of the abundant primary nuclei such as carbon and oxygen. Measurements of the secondary to primary ratios lead to the following conclusions [2]:

1. On average, CR in the GeV range traverse 5 - 10 g/cm^2 equivalent of hydrogen between injection and observation.
2. This effective grammage decreases as the energy increases.

Since the amount of matter along the line of sight through the disk of the Galaxy is about 10^{-3} g/cm^2 , this implies that cosmic rays travel during their lifetimes distances thousands of times greater than the thickness of the disk. This suggests diffusion in a containment volume that includes some or all of the disk of the Galaxy. The fact that the amount of matter traversed decreases as energy increases suggests that higher energy CR spend less time in the Galaxy than the lower energy ones. It also suggests that CR are accelerated before most of the propagation occurs [2].

CR particle trajectories are bent and scattered by the regular and chaotic magnetic fields and this produces a diffusive motion of CR in the galaxy [1]. A measure of deflection suffered by a particle is the ratio of its Larmor radius r_g and the typical scale of a volume with given magnetic field B . For a relativistic particle the Larmor radius is [4]:

$$r_g[m] = \frac{pc \sin \theta}{Ze Bc} \quad (3.2)$$

or

$$r_g[\text{pc}] \simeq \frac{E[10^{15} \text{eV}]}{ZB[\mu\text{G}]} \sin \theta \quad (3.3)$$

for the motion of the particle with the charge $Q = Ze$ (Z is atomic number) and constant energy E moving in a spiral path with constant pitch angle θ (the angle between vectors of the relativistic three-momentum \vec{p} and of the magnetic field \vec{B} vectors).

For a relativistic proton the Larmor radius is [4]:

$$r_g[m] = 3 \times 10^9 \gamma \left(\frac{B}{10^{-9} \text{T}} \right) \quad (3.4)$$

where the magnetic field strength B is measured in Tesla and γ is the Lorentz factor. Therefore, adopting the local value of the magnetic field strength in the interplanetary medium $B \approx 10^{-9}$ T, relativistic protons with $\gamma = 10^3$ (i.e. energies 10^{12} eV) have Larmor radii which are 3×10^{12} m = 20 AU, i.e. 20 times the distance from the Sun to the Earth [4].

3.4 Anisotropy

At energies smaller than 1 EeV, we expect near isotropy for galactic sources because of the diffusion of particles in the chaotic and regular galactic field. The cosmic ray anisotropy is conventionally defined as [1]:

$$\delta = \frac{I_{max} - I_{min}}{I_{max} + I_{min}} \quad (3.5)$$

where I_{max} and I_{min} are the maximum and minimum intensities of CR across the sky as a function of some coordinate. Parameter δ can be understood as a deviation from isotropy.

Some results have been presented on the anisotropy of the CR flux above $\approx 10^{17}$ eV from Fly's Eye and AGASA experiments. Both experiments report a small but statistically significant anisotropy of the order of 4% in terms of eq. (3.5) toward the Galactic plane at energies around 10^{18} eV. These analyses did not reveal a significant correlation with the Supergalactic Plane, whereas earlier work seemed to indicate some enhancement of the flux from this plane [5].

Anisotropy beyond 60 EeV

The Pierre Auger Observatory (PAO) demonstrates that there is a correlation between the arrival directions of CRs with energy above $\sim 6 \times 10^{19}$ eV and the positions of active galactic nuclei (AGN) lying within ~ 75 Mpc. They rejected the hypothesis of an isotropic distribution of these CR at over 99 % confidence level. The correlation is compatible with the hypothesis that the highest energy particles originate from nearby extragalactic sources whose flux has not been significantly reduced by interaction with

the cosmic background radiation. AGN or objects having a similar spatial distribution are possible sources. [6]

3.5 Origin of cosmic rays

Depending on the way, how the particle may reach its energy, there are two classes of models of acceleration. These classes are called "bottom-up" and "top-down model".

3.5.1 Bottom-up models

This scenario supposes, that final energy of CR particle is reached by stepwise acceleration by various astrophysical mechanisms. These astrophysical mechanisms (objects) include supernova remnants, radio galaxies, active galactic nuclei, neutron stars, gamma ray bursts, etc. Some of these astrophysical objects will be described in the following text.

Supernova remnants

A supernova remnant (SNR, see fig. 3.5) is the structure resulting from the gigantic explosion of a supernova. The supernova remnant is bounded by an expanding shock wave, and it consists of ejected material expanding from the explosion, and the interstellar material it sweeps up and shocks along the way [45]. SNRs are extremely important for understanding our Galaxy. They heat up the interstellar medium, distribute heavy elements throughout the Galaxy and accelerate cosmic rays [46].

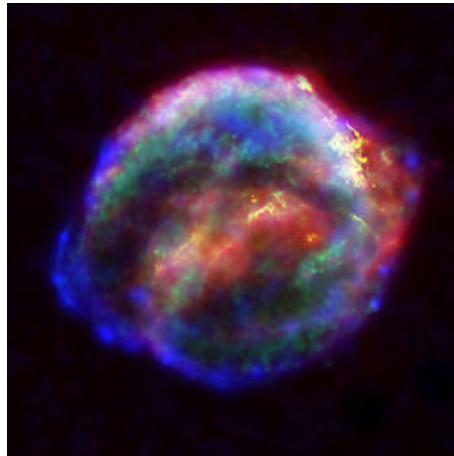


Figure 3.5: Remnant of Kepler's Supernova, SN 1604 [45].

The SNRs can be source of Galactic cosmic rays based on the shock acceleration. If supernova remnants are the sources capable of accelerating particles to $\sim 10^{15}$ eV or higher, then they should be also point sources of gamma-rays produced by interactions

of the accelerated particles in or near the source. The intensity depends on the degree of mixing between the high energy particles and ambient material. Theoretical estimates of the gamma-ray luminosity of SNRs caused by the π^0 -decay have led to the conclusion that the expected TeV gamma-ray flux from nearby SNRs is high enough and should be just detectable by present instruments [4]. The experimental proof that SNRs are actually accelerating particles to 10^{16} eV was established by the HESS experiment - TeV Cherenkov telescope recently built in Namibia [42].

Active galactic nuclei

Active galactic nuclei (AGN) are astrophysical objects, which have supermassive black hole in its center. This black hole is supplied by the material from surrounding accretion disk⁽⁶⁾ (see fig. 3.6).

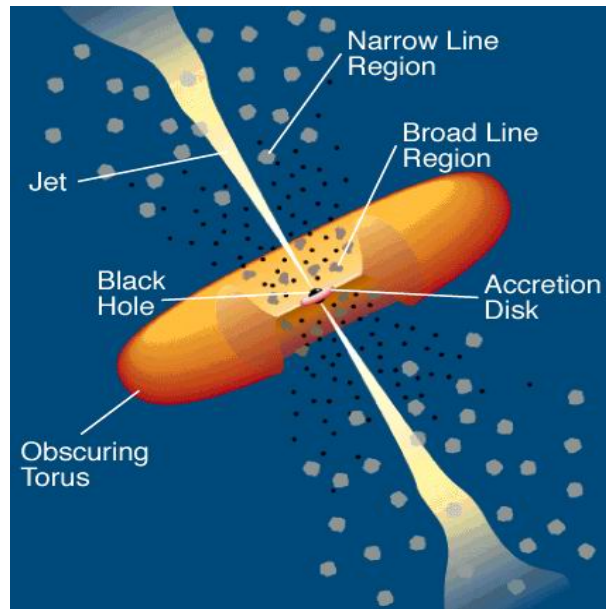


Figure 3.6: Active galactic nucleus.

From the inner part of accretion disk the most stridently ultraviolet and roentgen radiation are continuously coming out. The spectra of this object depend on the angle of the observation. If someone looks at this object from side, the inner part of accretion disk will cloud over the big part of radiation of AGN. A part of material is accelerated along the axis of symmetry and this material escapes like jets. It is supposed, that these jets are from both sides of AGN, but the radiation coming from the back jet is more reduced. The length of jets can reach a hundred of kpc. By the accretion of the matter to the central black hole a big amount of energy is produced.

⁶Accretion disk is composed of a matter, which is attracted into the central black hole.

As was mentioned above (in chapter 3.4.1), scientists from PAO discovered, that AGN lying close to Earth are possible sources of ultrahigh energy CR particles [6].

For the observer, the AGNs are different in these parameters: luminosity⁽⁷⁾, spectra, time variability and optical features.

Using their different characteristics the AGNs are usually classified into different groups: radio galaxies, quasars, blazars, Seyfert galaxies (type I. and II.), nuclear regions of ionized hydrogen (HII), galaxies with production of stars, etc. The most significant groups are listed and characterized below:

- **Quasars** are stars similar (its angular size is less than one angle second) extragalactic objects (usually with big red shift), which can be optically determined by wide spectral lines (which correspond to high speed of thermal gases).
- **Blazars** are very shining and highly varying extragalactic objects. The jets point directly towards the observer. Blazars are highly varying in spectral regions of radio, optical and X-rays radiation. They don't show wide optical lines. The optical radiation from these objects is strongly and variously polarized.
- **Seyfert galaxies** are usually spiral galaxies. Strong activity of nuclei is typical for them. They have the following qualities: small and very clear nucleus, in their spectra a lot of wide emission spectral lines shine (the gas is fast moving, the speeds reaches 5000 km/s), they have non-thermal radiation in wide spectral range and in the nucleus there is very compact source of radio radiation.

Neutron stars

A neutron star is formed from the collapsed remnant of a massive star, a Type II, Type Ib, or Type Ic supernova and models predict that it consists mostly of neutrons. It is a very hot environment due to repulsion between neutrons as given by Pauli exclusion principle. A neutron star is one of the few possible conclusions of stellar evolution.

A typical neutron star has a mass between 1.35 and about 2.1 of solar masses, with a corresponding radius between 20 and 30 km - 30 000 to 70 000 times smaller than the Sun. Typical neutron stars have densities of about 10^{14} g/cm³.

Gamma ray bursts

Gamma-ray bursts (GRBs) are short-lived bursts of gamma-ray photons. At least some of them are associated with a special type of supernovae, respectively supernova explosions of super massive stars.

Lasting from a few milliseconds to several minutes, gamma-ray bursts shine hundreds of times brighter than a typical supernova and about a million trillion times brighter than the Sun. This makes them briefly the brightest source of cosmic gamma-ray photons in the observable Universe. GRBs are detected roughly once per day from random directions of the sky.

Cosmological GRBs most likely contribute a negligible fraction to the low energy CR flux around 100 GeV, as compared to SNRs, the favorite CR source below the

⁷Shiny energy output.

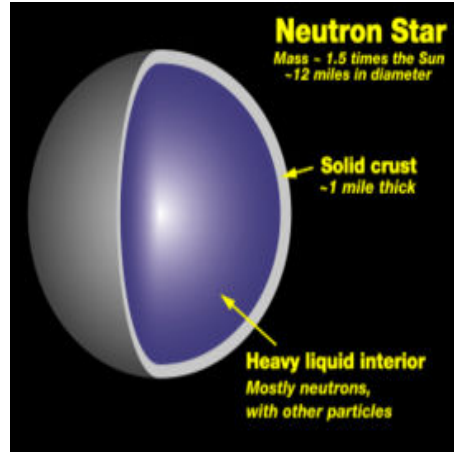


Figure 3.7: A model of neutron star internal structure [43].

knee. In contrast, a possible common origin of UHECR and cosmological GRBs, mainly based on the observation that the average rate of energy emission required to explain the observed UHECR flux is comparable to the average rate of energy emitted by GRBs in γ -rays. The predicted spectrum seems to be consistent with the observed spectrum above $\approx 10^{19}$ eV for proton injection spectra $\propto E^{-2.3 \pm 0.5}$, typical for the Fermi acceleration mechanism which is supposed to operate in dissipative wind models of GRBs. However in recent studies the origin of UHECR from GRB seems to be improbable [7].

3.5.2 Top-down models

The shock acceleration mechanism is a self-limiting process: For any given set of values of the dimension of the acceleration region (fixed by, say, the radius R of the shock) and the magnetic field strength B , simple criterion of Larmor containment of a particle of charge Ze within the acceleration region implies that there is a maximum energy $E_{max} \approx ZeBR$ up to which the particle can be accelerated before it escapes from the acceleration region. [5]. The mechanism thus prevents further acceleration to energies higher than E_{max} .

The basic idea of top-down models⁽⁸⁾ is, that extremely high energy cosmic ray (UHECR) particles need not to be produced by any acceleration mechanism at all; instead, these particles may simply be the result of a decay of certain massive particles (generically "X" particles) with mass $m_X > 10^{11}$ GeV originating from high energy processes in the early Universe.

In the modern version of the top-down scenario of cosmic ray origin, the X particles typically decay to quarks and leptons. The quarks hadronize, i.e., produce jets of hadrons containing mainly light mesons (pions) with a small percentage of baryons

⁸Top-down model is non acceleration and is opposite to conventional bottom-up acceleration mechanisms.

(mainly nucleons). The pions decay to photons, neutrinos (and antineutrinos) and electrons (and positrons). Thus, energetic photons, neutrinos and charged leptons, together with a small fraction of nucleons, are produced directly with energies up to $\approx m_X$ without any acceleration mechanism [5].

3.6 Acceleration mechanism

As was already mentioned above (chapter 3.5), there are two classes of CR origin - the bottom-up and top-down models. In this section we will describe acceleration models for bottom-up scenario. These accelerations models can be divided into two groups: Fermi acceleration and direct acceleration.

In the case of Fermi acceleration model the multiple collisions with the magnetic fields of moving clouds or shock waves are responsible for the gain of particle final energy. The time, which is necessary for the particle to reach its energy, can be even thousands of years. The basic principle of this acceleration mechanism was proposed by Enrico Fermi in the year 1949. This mechanism will be labeled as Fermi II⁽⁹⁾.

In the year 1978, Bell, Blandford and Ostriker, have applied Fermi's original theory to fast moving shock waves. In this case, the final energy reaches higher values and the acceleration time is shorter, thus the mechanism is more effective than the Fermi II. This mechanism will be labeled as Fermi I⁽¹⁰⁾.

3.6.1 Fermi's original theory (Fermi II)

Fermi supposed, that particles are accelerated by collisions with magnetic clouds in the Galaxy. The energies of these magnetic clouds are much higher than the particle energy, which collides with these clouds during acceleration mechanism.

Fermi II acceleration mechanism is based on following assumptions:

- The particle is relativistic ($E = pc$).
- We neglect the energetic losses during scattering. (The assumption of elastic scattering.)
- The particle is moving randomly in the magnetic cloud.
- The structure of magnetic cloud is given and it isn't influenced by the collisions with particles.

For the scheme where the particle scattering on the magnetic cloud see fig. (3.8). The moving particle has initial energy E_1 (on the beginning of the process) and θ_1 is the angle between velocity vectors of magnetic cloud and particle. E_2 is the final energy of particle (at the end of the process) and the particle flies out under the angle θ_2 . The magnetic cloud moves slowly with the velocity \vec{V} . All quantities are labeled in the laboratory frame. Let us label the quantities in the rest frame like (E'_1, \dots) .

⁹The reason is that the energy gain per one scattering is proportional to β . β is characteristic velocity of moving cloud or shock wave.

¹⁰Due to the energy gain per one scattering proportional to β

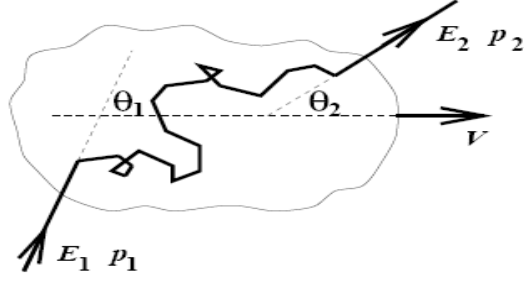


Figure 3.8: The scheme of the CR particle scattering on the magnetic cloud. This picture was taken from [8].

$$\begin{pmatrix} \frac{i}{c}E'_1 \\ p'_1 \\ 0 \\ 0 \end{pmatrix} = \begin{pmatrix} \gamma & -i\beta\gamma & 0 & 0 \\ i\beta\gamma & \gamma & 0 & 0 \\ 0 & 0 & 1 & 0 \\ 0 & 0 & 0 & 1 \end{pmatrix} \begin{pmatrix} \frac{i}{c}E_1 \\ p_1 \cos \theta_1 \\ 0 \\ 0 \end{pmatrix} \quad (3.6)$$

$$\begin{pmatrix} \frac{i}{c}E_2 \\ p_2 \\ 0 \\ 0 \end{pmatrix} = \begin{pmatrix} \gamma & i\beta\gamma & 0 & 0 \\ -i\beta\gamma & \gamma & 0 & 0 \\ 0 & 0 & 1 & 0 \\ 0 & 0 & 0 & 1 \end{pmatrix} \begin{pmatrix} \frac{i}{c}E'_2 \\ p'_2 \cos \theta'_2 \\ 0 \\ 0 \end{pmatrix} \quad (3.7)$$

Using Lorentz transformation from the laboratory frame to rest frame (3.6) one can obtain equation:

$$E'_1 = \gamma E_1 (1 - \beta \cos \theta_1), \quad (3.8)$$

where $\beta = V/c$ a $\gamma = 1/\sqrt{1 - \beta^2}$.

Using Lorentz transformation from the rest frame to laboratory frame (3.7) one can obtain equation:

$$E_2 = \gamma E'_2 (1 + \beta \cos \theta'_2). \quad (3.9)$$

Due to the assumption of elastic scattering, the energy in the rest frame will conserved $\Rightarrow E'_1 = E'_2$ and following equation can be obtained:

$$E_2 = \gamma^2 E_1 (1 - \beta \cos \theta_1)(1 + \beta \cos \theta'_2). \quad (3.10)$$

The equation (3.10) can be overwritten to energy gain per one collision $(E_2 - E_1)/E_1$, hence we obtain the following equation:

$$\frac{E_2 - E_1}{E_1} = \frac{\Delta E}{E_1} = \gamma^2 (1 - \beta \cos \theta_1)(1 + \beta \cos \theta'_2). \quad (3.11)$$

Because the particle movement is random in magnetic cloud, all possible values of the θ'_2 angle will have the same probability. From this can be shown, that:

$$\langle \cos \theta'_2 \rangle = 0. \quad (3.12)$$

The average value of $\cos \theta_1$ depends on the rate at which CR collide with clouds at different angles. The rate of collision is proportional to the relative velocity between the cloud and the particle so that the probability per unit solid angle of having the collision at angle θ_1 is proportional to $(v - V \cos \theta_1)$ and for ultrarelativistic particles ($v \approx c$) thus leads to [8]:

$$\langle \cos \theta_1 \rangle = -\frac{\beta}{3}. \quad (3.13)$$

The mean value of equation (3.11) over all angles leads to:

$$\frac{\Delta E}{E_1} \approx \frac{4}{3} \beta^2. \quad (3.14)$$

Because of $\beta \ll 1$, the average energy gain per one collision is very small. The energy gain is so small due to two possibilities of the collision. The first one is catch-up collision (the particle loses its energy) and the second one is head-on collision (the particle gain energy). It can be shown, that probability of head-on collision is higher than the probability of catch-up collision and on average the resulting energy of particle is higher than initial energy of particle [1].

3.6.2 First order Fermi acceleration (Fermi I)

Due to the long time, which was needed to accelerate the particle to the highest energies (the particle was confined for a long time in magnetic cloud), Fermi's original theory was modified in the seventies. This mechanism is important in shock waves from supernova, but it is generally applicable to any stronger shock waves from other astrophysical objects [4].

In this case, the head collision happened between shock wave and relativistic particle (see fig. 3.9). Shock wave is created by the explosion of supernova. By this explosion several solar masses are ejected with the speed of about 10^4 km/s, which is higher than speed of sound in interstellar space (10 km/s) [4]. The velocity of this shock wave is labeled as $-\vec{u}_1$. The particle is moving towards to shock wave by the velocity \vec{u}_2 and $|u_1| > |u_2|$. The particle velocity behind shock wave in the laboratory frame of the shock is $\vec{V} = -\vec{u}_1 + \vec{u}_2$, and it can be interpreted as the velocity of accelerated particle ("downstream") with regard to unaccelerated particle ("upstream").

Like in the Fermi's original theory, the mean value of $\cos \theta_1$ and $\cos \theta'_2$ can be determined. But, in the first order Fermi acceleration, the mean value of $\cos \theta'_2$ is not zero. It can be shown, that in this case, the mean values are:

$$\langle \cos \theta_1 \rangle = -\frac{2}{3}, \quad (3.15)$$

$$\langle \cos \theta'_2 \rangle = \frac{2}{3}. \quad (3.16)$$

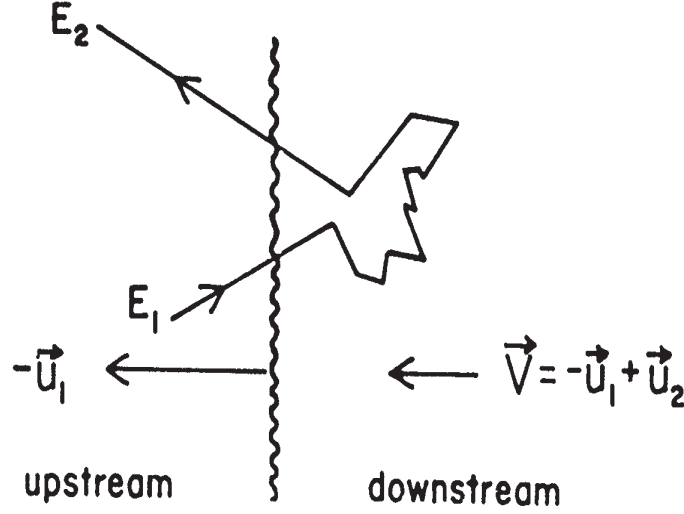


Figure 3.9: The scheme of first order Fermi acceleration [2].

Using equations (3.15), (3.16) and (3.11) one can obtain:

$$\frac{\Delta E}{E_1} = \frac{1 + 4\beta/3 + 4\beta^2/9}{1 - \beta^2} - 1 \approx \frac{4}{3}\beta. \quad (3.17)$$

The energetic gain depends linearly on $\beta = V/c$. Here β refers to the relative velocity of the plasma flow, not of the CR. The equations (3.17) and (3.14) are valid only for non-relativistic shock waves but it can be shown that similar results can be obtained in the case of the relativistic moving shock wave, too.

In this case the acceleration mechanism is more efficient because of the non-random movement of the particle in the magnetic cloud. In this process, the collision of the particle with the shock leads always to the energetic gain.

3.6.3 Spectral index

The result of Fermi acceleration is the universal power-law spectrum of the accelerated particles. It can be written in a differential form:

$$\frac{dN(E)}{dE} \approx E^{-q}, \quad (3.18)$$

or in an integral form:

$$N \approx E^{-(q-1)}. \quad (3.19)$$

Here we define differential spectral index [4]:

$$q = \frac{R+2}{R-1}, \quad (3.20)$$

where

$$R = \frac{u_1}{u_2} \quad (3.21)$$

is the shock compression ratio, u_1 and u_2 being the upstream and downstream velocities of the fluid in the rest frame of the shock. For typical situation is $R < 4$ and hence $q > 2$ ($q = 2$ for the strong shocks).

The effectively continuous gain of energy can be characterized as:

$$\frac{dE}{dt} = \frac{\langle \Delta E \rangle}{t_{cycle}}, \quad (3.22)$$

where t_{cycle} is the time for one complete cycle (i.e. from crossing the shock from upstream to downstream, diffusing back towards the shock and crossing from downstream to upstream, and finally returning to the shock), and $\langle \Delta E \rangle$ is the average energy gain per cycle.

3.6.4 Direct acceleration

Particles can be accelerated directly in objects with large electric potential, like neutron stars or accretion disks of black holes.

On the surface of young, fast rotating⁽¹¹⁾ neutron stars, the magnetic field can reach 10^8 T and induced electric potential can reach 10^{18} V. If there would be no collisions⁽¹²⁾ (there will be no energetic losses), the particles can be accelerated to the energy:

$$E = Z \times 10^{18} [eV]$$

where Z is the particle charge.

3.6.5 Hillas condition

Irrespective of the precise acceleration mechanism, there is a simple dimensional argument, given by Hillas, which allows one to restrict attention to only a few classes of astrophysical objects as possible sources capable of accelerating particles to a given energy. To keep the particle confined within the acceleration region the magnetic field B is needed. Thus, the size R of the acceleration region must be larger than the diameter of the orbit of the particle $\sim 2r_g$. Including the effect of the characteristic velocity βc of the magnetic scattering centers one gets the general condition [5], [9]:

$$\left(\frac{B}{\mu G} \right) \left(\frac{R}{\text{kpc}} \right) > 2 \left(\frac{E}{10^{18} eV} \right) \frac{1}{Z\beta}. \quad (3.23)$$

The equation (eq. 3.23) is often presented in the form of the famous "Hillas diagram" (see fig. 3.10), which shows that to achieve a given maximum energy, one must have acceleration region that have either a large magnetic field or a large size of

¹¹With rotational frequency about 30 s^{-1} .

¹²But there is problem, that the environment around these objects has high density, so the particle suffer energetic losses.

the acceleration region. Thus, for example, only a few astrophysical sources - among them, AGNs, radio-galaxies, and pulsars - satisfy the necessary conditions (but may or may not be sufficient) for acceleration up to $\sim 10^{20}$ eV [5].

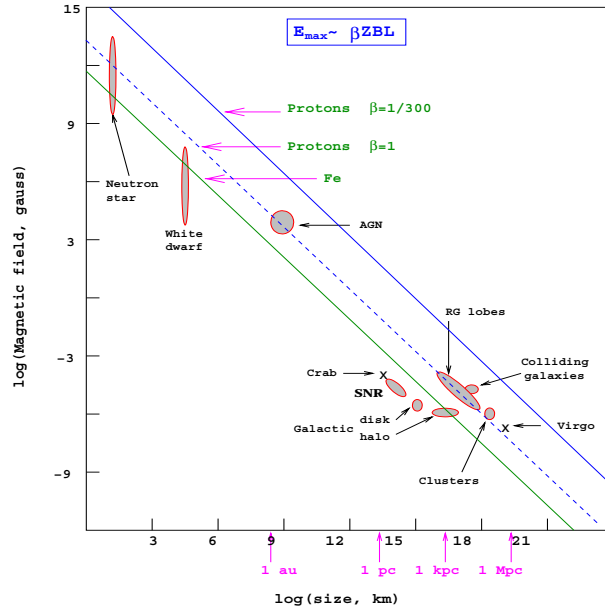


Figure 3.10: The Hillas diagram showing size and magnetic field strengths of possible sites of particle acceleration. Objects below the corresponding diagonal lines cannot accelerate protons (iron nuclei) to 10^{20} eV. βc is the characteristic velocity of the magnetic scattering centers [5]. The upper diagonal line is for protons $\beta = 1/300$, the middle diagonal line is for protons $\beta = 1$ and the lower diagonal line is for Fe nuclei. This picture was taken from [5].

3.7 Galactic and extragalactic cosmic ray

3.7.1 Galactic cosmic ray

While solar CR are identified by their temporal association with solar flares or spatial association with interplanetary shocks, or by the compositional and spectral signatures of anomalous CR, the steady, nearly isotropic flux of high energy particles comes from sources far outside the heliosphere. These sources still lack definitive identification nearly a century after their discovery. The fundamental difficulty is that diffusive propagation in the turbulent interstellar medium smooths out spatial and temporal variations that may characterize the sources [10].

It is generally believed that the bulk of CRs with energy below the knee are Galactic in origin and that their main production mechanism is acceleration by supernova shocks [2].

The knee of the spectrum

One interpretation of the knee of the spectrum is that it reflects a change in propagation of galactic CRs, perhaps corresponding to more rapid escape from the galaxy. A problem of this interpretation is that the spectrum in the knee region may have more structure than would be the case for a steepening of the rigidity spectrum of each elemental component of CR. An alternate interpretation is that this part of the spectrum may be produced by only one or a few sources [10].

Another and maybe more probable explanation of the origin of the knee is that SNRs are not able to accelerate particles to higher energies. The continuous break in the spectrum (knee) is caused by the fact, that energies, which can reach protons from SRNs are lower, than energies of heavier nuclei. If the maximal energy to which particles can be accelerated in SNRs is about the energy of the knee, the composition of CRs is also changing at this point of spectra.

3.7.2 Extragalactic cosmic ray

Ultra high energy cosmic rays are presumed to be of extragalactic origin. With increasing energies, and thus Larmor radii⁽¹³⁾, the galactic charged particles can not be confined in our Galaxy. Moreover the accelerator candidates in the Galaxy are expected to reach their maximum energy well below 10^{18} eV [11].

3.7.3 Transition from galactic to extragalactic

The transition between galactic and extragalactic cosmic rays is believed to happen between 10^{18} and 10^{19} eV where a spectral break in the CR flux known as the 'ankle' or 'dip' is observed. The exact position and nature of the transition is still disputed and it seems clear that a combined precise measurement of the particle flux and composition in this energy range is needed to be able to distinguish between different models of the extragalactic cosmic ray component [11].

3.8 GZK cut-off

In the year 1966 K. Greisen [12] and independently G. T. Zatsepin and V. A. Kuzmin [13] showed that CRs particles lose their energy by interactions with cosmic microwave background (CMB) radiation. The relict photons (CMB) remain after Big Bang⁽¹⁴⁾. Today they have a temperature of 2.7 K. This radiation (CMB) homogenously fills all the Universe and has big influence on the propagation of the CR's particles with extremely high energies. The existence or non-existence of GZK cut-off is one of the fundamental questions of current studies of CR (see fig. (3.11) - the different results of experiments AGASA and HIRes).

The principal reactions of protons p with background photons ($\gamma_{2.7K}$) are [14]:

¹³Larmor radii become larger than the thickness of Galactic disk.

¹⁴The beginning of our Universe.

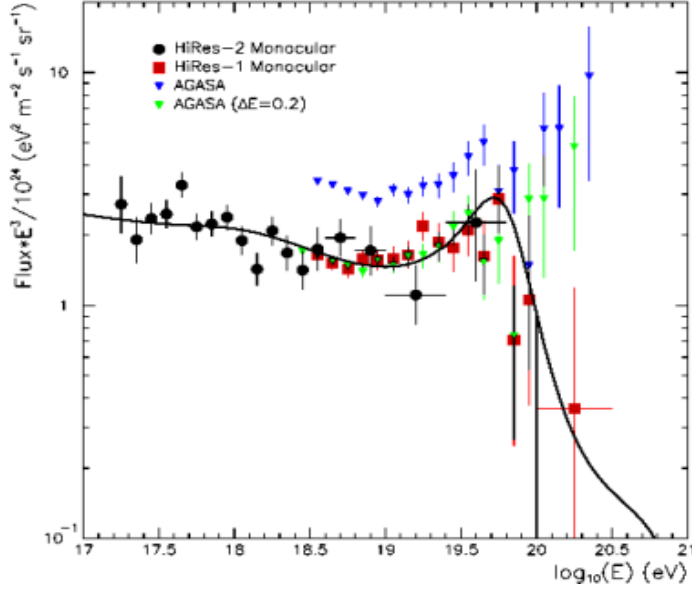
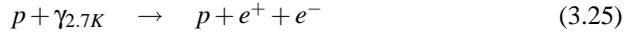


Figure 3.11: The comparison of measurement of the end of the energetic spectra of cosmic rays from the experiments HIRes and AGASA. Black circles and red squares are the results of HIRes. The green and blue triangles are the results from AGASA. Despite that AGASA observes the continuous spectrum (no evidence of GZK cut off), the experiment HIRes observes the steep slope of the spectrum end (evidence of GZK cut off).



For a background photon of energy ϵ in the CRF (CRF - cosmic rest frame, defined as the frame in which the CMB is isotropic), the threshold energy of photo-pion (see equation 3.24) production ($N\gamma_b \rightarrow N(n\pi), n \geq 1$) for the nucleon energy is [5]:

$$E_{th} = \frac{m_\pi(m_N + m_\pi/2)}{\epsilon} \approx 6.8 \times 10^{16} \left(\frac{\epsilon}{\text{eV}}\right)^{-1} \text{ eV},
 \tag{3.26}$$

where m_N is nucleon mass and m_π is pion mass. Energy loss per interaction is around 20 % [14].

Typical CMB photon energies are $\epsilon \sim 10^{-3}$ eV, leading to the so called Greisen-Zatsepin-Kuzmin (GZK) "cutoff" at a several tens of EeV [5].

From the fig. (3.12) one can clearly see, how the GZK cut-off threshold "works". If any UHECR particle traveled sufficient distance, the energy of the particle decreases to the GZK cut-off independently on the initial energy of the particle.

Other energetic losses of UHECR

Below this energy range, the dominant loss mechanism for protons is production of electron-positron pairs on the CMB (see equation 3.25 - in this case the energy loss per interaction is "only" around 0.1 % [14]), $p\gamma_b \rightarrow pe^+e^-$, down to the corresponding threshold [5]:

$$E_{th} = \frac{m_e(m_N + m_e)}{\epsilon} \approx 4.8 \times 10^{14} \left(\frac{\epsilon}{\text{eV}} \right)^{-1} \text{ eV.} \quad (3.27)$$

Therefore, pair production by protons (PPP) in the CMB ensues at a proton energy $E \sim 5 \times 10^{17}$ eV.

The next important energy loss mechanism which starts to be dominant near and below PPP threshold is redshifting due to the cosmic expansion. All other energy loss processes are negligible, except possibly in very dense central regions of galaxies [5].

For neutrons, β -decay ($n \rightarrow pe^-\bar{\nu}_e$) is the dominant process for $E \leq 10^{20}$ eV. The neutron decay rate $\Gamma_n = m_N/(\tau_n e)$, with $\tau_n \approx 888.6 \pm 3.5$ sec the laboratory lifetime, implies for neutrons range of propagation [5]:

$$R_n = \tau_n \frac{E}{m_N} \approx 0.9 \left(\frac{E}{10^{20} \text{ eV}} \right) \text{ Mpc.} \quad (3.28)$$

where E is neutron energy and m_N is neutron mass.

The dominant energy loss process for nuclei of energy $E \geq 10^{19}$ eV is photodisintegration in the CMB and the IR background (IRB) due to the giant dipole resonance [5].

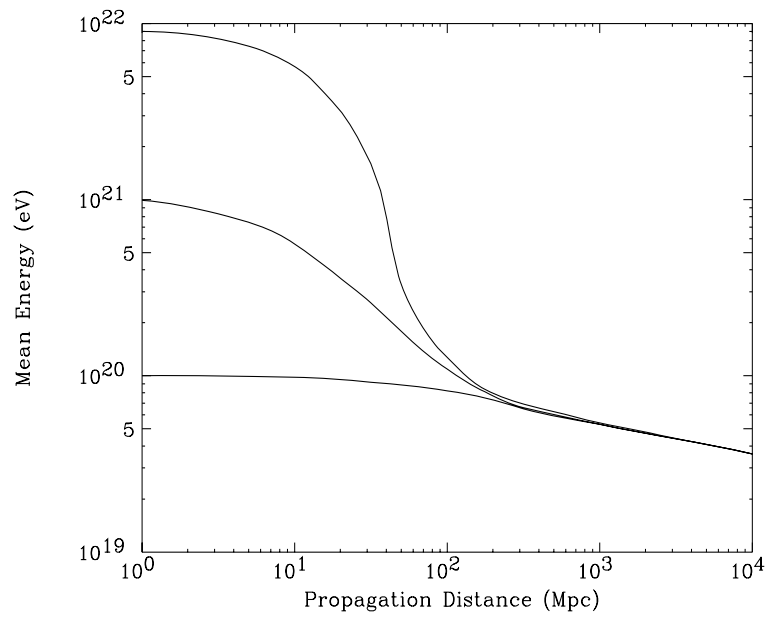


Figure 3.12: The scheme of the energy losses of CR particles as a function of the distance traveled. This picture was taken from [15].

Chapter 4

Secondary Cosmic Rays

4.1 Basic description and features

If the primary cosmic ray particle hits the Earth's atmosphere, this particle interacts with the atmospheric nuclei. The reaction chain starts. In this reaction chain - so called **shower of secondary particles** - many new particles are created (see the fig. 4.1 for illustration). This particle cascade is also called extensive air shower (EAS).

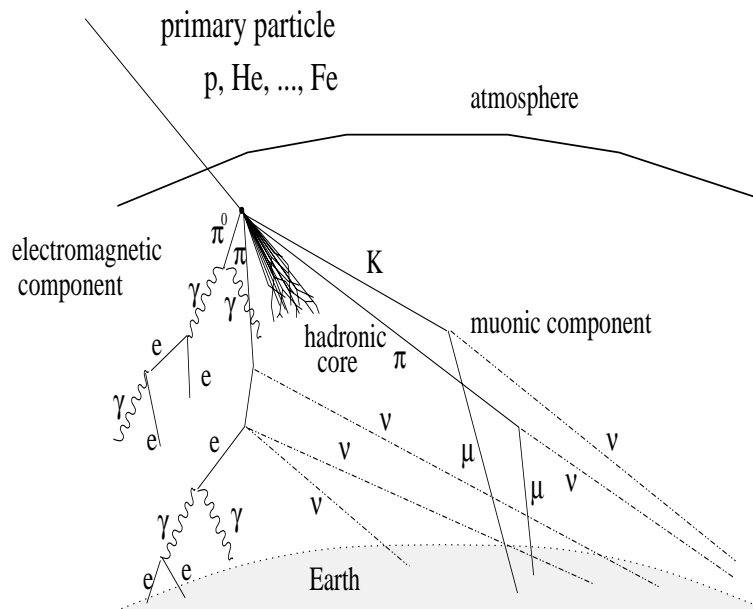


Figure 4.1: Illustration of the components of the shower of the secondary particles. This picture is taken from [16].

The first interaction occurs at altitude of a few tens of kilometers. The position of the first interaction is strongly dependent on the type of the primary particle and its energy.

The EAS may have millions till a few tens of billions secondary particles. The number of these secondary particles depends on the positions of the first interactions, on the type of the primary particle, on its energy and also on the altitude. The number of the secondary particles increases from the first interaction. In a few kilometers above sea level, the shower reaches its maximum. It happens, when the average energy per particle decreases under critical value of energy⁽¹⁾. Under this critical energy a creation of new particles is no longer possible. This point is called *the maximum of the shower*⁽²⁾.

In some assumptions, it is supposed, that the shower front is planar and it looks like a pancake. When the shower falls down to the Earth's surface it may have a few kilometers in diameter. So the shower can hit the area of few tens of km². The size of this area is strongly dependent on the zenith angle⁽³⁾.

On the Earth's surface, only secondary particles can be detected. Because of the big diameter of the shower from the primary particles with the highest energies, the big area must be covered by detectors⁽⁴⁾. From the secondary particles, which are detected, the type of primary particle, the arrival direction and its energy can be determined.

The composition of the EAS depends on the primary particle. If the primary particle is photon, the EAS will be composed almost from electrons, positrons and photons. If the primary particle is some nucleus, the shower will be composed furthermore from muons, neutrinos and hadrons (protons, neutrons and pions).

The shower has three components, which will be described in the next sections. There are electromagnetic, hadronic and muonic components.

The shower consists of a core of high energy hadrons. This hadronic core continually feeds the electromagnetic part of the shower, primarily by the photons from decay of the neutral pions and eta particles. Nucleons and other high energy hadrons contribute further to the hadronic cascade. Lower energy charged pions and kaons decay to feed the muonic component [2].

¹This energy is called *critical energy* E_c .

²Maximum of the shower - in the sense of the number of the particles. There can be also maximum of the shower in the sense of energy loss. Both maxima occur close together.

³The zenith angle is the angle between the line, which is perpendicular to Earth's surface and between the direction, from which the particle comes.

⁴And also the main reason for a big covered area is the small flux of UHECR.

4.2 Toy model

A very simple model by Heitler (1944) illustrates some general features of air showers. Heitler introduced this model for development of electromagnetic cascade, but the basic structure is also applicable to air shower initiated by hadrons [2].

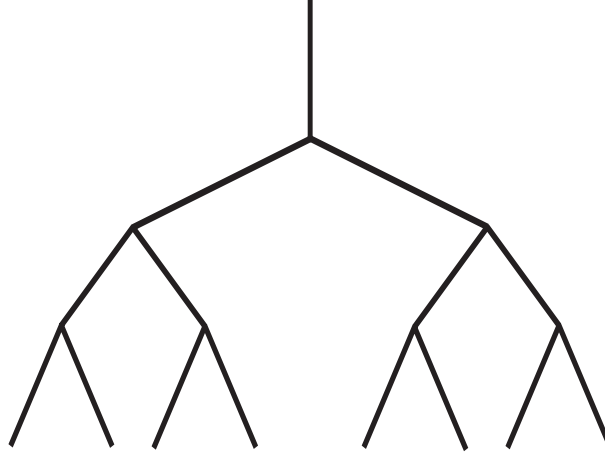


Figure 4.2: Simple branching model of an air shower.

The scheme of this model is in the picture (4.2). Each line represents a "particle" or a packet of energy. After one collision length λ the line splits into two lines. This is branching process.

After $n = X/\lambda$ collisions, the number of the particle is:

$$N(X) = 2^n = 2^{X/\lambda}, \quad (4.1)$$

where X is slant depth along the shower axis.

At the depth X the energy per one particle is equal to:

$$E(X) = E_0/N(X), \quad (4.2)$$

where E_0 is primary particle energy.

The splitting continues until $E(X) = E_c$, where E_c is the critical energy for given process. After this, the particle only loses its energy - gets absorbed, or decays.

The number of particles at shower maximum is equal to:

$$N_{max} = E_0/E_c, \quad (4.3)$$

and it can be shown, that the position of maximum of the shower can be determined as:

$$X_{max} = \lambda \frac{\ln(E_0/E_c)}{\ln 2}. \quad (4.4)$$

Equation (4.3) and (4.4) hold not only for electromagnetic cascades, but approximately also for showers induced by hadrons (i.e. for CR showers as well) namely:

$$N_{max} \propto E_0 \quad \text{and} \quad X_{max} \propto \ln(E_0). \quad (4.5)$$

These equations may help us to understand behavior of X_{max} as a function of E as will be studied in details in the chapter 8.

4.3 The shower components

Electromagnetic component

The electromagnetic component is composed of electrons, positrons and photons. The basic high-energy processes, which contribute to the electromagnetic component are pair production and bremsstrahlung.

The number of e^+ , e^- and γ increases until the energy of such particles is higher than critical energy ($E > E_c$). The critical energy for electrons in the air is approximately equal to 80 MeV. Below this critical energy, the numbers of e^+ , e^- and γ rapidly decrease.

Above the energy $E > E_c$, collision losses and Compton scattering can be neglected in calculating the shower development [2].

The radiation length for electrons in the air is equal to 37.1 g/cm^2 . The energy loss due to bremsstrahlung is: $\frac{dE}{dX} \approx -\frac{E}{X_0}$, here X_0 is the radiation length for electrons in air.

Hadronic component

In the hadronic component, there are predominantly nucleons, pions and kaons. This component of EAS is increasing its strength until the energy of nucleons decreases under the value of energy of a few hundreds of MeV. Protons lose their energy in ionization processes and neutrons evoke nuclear processes until they become slow. Slow neutrons are then captured, mostly by ^{14}N nucleus [17]. ($^{14}\text{N}(n, p)^{14}\text{C}^*$)

Muonic component

Muons in the shower originate predominantly from the decays of pions and kaons. Muons are considered as more penetrating component of the shower.

The probability that pions more likely decay than interact depends on the energy of the primary particle and the density of the atmosphere. In the higher parts of the atmosphere, due to the lower density, the probability of decay of high-energetic pions is high. The most energetic muons are the results of the high-energetic pions and they give us an information about the earlier development of the shower. High-energetic muons are produced near the shower axis and they are created approximately at the altitude of 8 - 16 km above sea level [1].

The numbers of high-energetic (in the order of TeV) and low-energetic (in order of GeV) muons depend on the atomic number of the primary particle.

Let us suppose, for example, two showers. Both with the same primary energy, but in the first one primary particle is proton, and for the second one the primary particle is iron nucleus. In the interaction of iron nuclei with the atmosphere, approximately 56 subshowers is created. Each subshower is generated by the nucleon with average energy $E_0/56$. The heavier primary nuclei create more pions, but with lower average energy. Most of these pions will decay to the muons.

Number of the high-energy muons created by the primary particle with atomic number A can be determined from this formula [1]:

$$N_{\mu}(> E_{min}) = \frac{KA \sec \theta}{E_{min}} \left(\frac{E_{min}}{E_0/A} \right)^{\alpha} \left(1 - \frac{E_{min}}{E_0/A} \right)^{\beta}, \quad (4.6)$$

where E_0 is energy of primary particle in GeV, A is atomic number of primary particle, E_{min} is in units of GeV, $K = 14.5$ GeV, $\alpha = -0.757$, $\beta = 5.25$, θ is zenith angle. This equation is based on Monte-Carlo simulation and it is supposed that $\theta < 60^\circ$.

4.4 The development of the shower

In the shower, there are stable and unstable particles, which can be charged or neutral. Unstable particles can interact or decay, stable particle can only interact. Between two interactions (or decay) the charged particle loses its energy by ionization processes (or by excitation - will be described later in this section). Neutral particle does not suffer any energetic losses between interactions (or decay).

The distance traveled by a particle before it undergoes its next inelastic interaction or decay can be determined by the cross section for a hadronic reaction and the probability of decay [18].

4.4.1 Ionization energy loss

The energy loss by ionization of a charged particle which traverses matter of thickness λ is described by the Bethe-Bloch stopping power formula [18]:

$$dE_i = \frac{\lambda z^2}{\beta^2} \kappa_1 (\ln(\gamma^2 - 1) - \beta^2 + \kappa_2) = \frac{\lambda \gamma^2 z^2}{\gamma^2 - 1} \kappa_1 (\ln(\gamma^2 - 1) - \beta^2 + \kappa_2) \quad (4.7)$$

where $\beta = v/c$ is the velocity of the particle in the laboratory frame in the units of the speed of light, γ is its Lorentz factor, z is the charge of the ionizing particle in units of e and κ_1 and κ_2 are constants for air in units [$\text{MeVg}^{-1}\text{cm}^2$].

4.4.2 Particle decays

Most of the particles, which are produced in high-energy interactions are unstable and they may decay into other stable or unstable particles. Neutral pions and η mesons and all resonances have short life time, so their interactions are negligible - only decays are important. The only way, which prevents the muons to penetrate through the

atmosphere is decay. In CR shower neutrons can be considered as a stable particles, due to their long life time. For all other unstable particles, there is a competition between decays and interactions⁽⁵⁾.

π^0 decays

The dominant decay process for neutral pions is the decay into two gamma:

$$\pi^0 \rightarrow \gamma + \gamma.$$

The probability of this decay is 98.8%. This decay is isotropic in central mass system of π^0 . Thus the energy of γ is equal to: $E_\gamma = m_{\pi^0}c^2/2$.

Other possibility, how neutral pion can decay is so called Dalitz decay:

$$\pi^0 \rightarrow e^+ + e^- + \gamma.$$

This decay has probability only 1.2 %.

The mean lifetime of π^0 is $(8.4 \pm 0.6) \times 10^{-17}$ s.

π^\pm decay

The decay process of charged pions is:

$$\pi^\pm \rightarrow \mu^\pm + \nu_\mu.$$

This decay is isotropic in the central mass system of the charged pion.

The mean lifetime of π^\pm is $(2.6033 \pm 0.0005) \times 10^{-8}$ s.

Muon decay

The decay process for muon is:

$$\mu^\pm \rightarrow e^\pm + \nu_e + \nu_\mu.$$

The mean lifetime of μ^\pm is $(2.19703 \pm 0.00004) \times 10^{-6}$ s.

Kaon decays

Kaons may decay by many ways. The final state consists mostly from two or three particles. The dominant decays and their probabilities are in the table (4.1).

The mean lifetime of K^\pm is $(1.2386 \pm 0.0024) \times 10^{-8}$ s, the mean lifetime of K_S^0 is $(0.8935 \pm 0.0008) \times 10^{-10}$ s and the mean lifetime of K_L^0 is $(5.17 \pm 0.04) \times 10^{-8}$ s.

η decays

The η mesons can decay in several ways, the most dominant processes are in the table (4.2).

The mean lifetime of η mesons is approximately 5×10^{-19} s.

⁵In this section (Particle decays) literatures [33] and [18] is used.

decay mode	probability [%]	decay mode	probability [%]
$K^\pm \rightarrow \mu^\pm + \nu$	63.5	$K_S^0 \rightarrow \pi^+ + \pi^-$	68.6
$K^\pm \rightarrow \pi^\pm + \pi^0$	21.2	$K_S^0 \rightarrow 2\pi^0$	31.4
$K^\pm \rightarrow \pi^\pm + \pi^\pm + \pi^\mp$	5.6	$K_L^0 \rightarrow \pi^\pm + e^\mp + \nu$	38.7
$K^\pm \rightarrow \pi^0 + e^\pm + \nu$	4.8	$K_L^0 \rightarrow \pi^\pm + \mu^\mp + \nu$	27.1
$K^\pm \rightarrow \pi^0 + \mu^\pm + \nu$	3.2	$K_L^0 \rightarrow 3\pi^0$	21.8
$K^\pm \rightarrow \pi^0 + \pi^0 + \pi^\pm$	1.7	$K_L^0 \rightarrow \pi^+ + \pi^- + \pi^0$	12.4

Table 4.1: The dominant decays of kaons.

decay mode	probability[%]
$\eta \rightarrow \gamma + \gamma$	39.13
$\eta \rightarrow 3\pi^0$	32.09
$\eta \rightarrow \pi^+ + \pi^- + \pi^0$	23.89
$\eta \rightarrow \pi^+ + \pi^- + \gamma$	4.94

Table 4.2: The dominant decays of η mesons.

Strange baryon and resonance decays

This decays are also well known and the branching ratios can be found e.g. in [18].

4.4.3 Particle interactions

Hadronic interaction

The hadrons are produced by strong interaction of the incoming primary particle and by further interactions. Hadrons interact with another air nuclei and create a new sub-shower. If the hadrons have small energy, they can only excite air nucleus.

Muonic interactions

Muons suffer energetic losses by bremsstrahlung or by e^+e^- -pair production. Both processes are negligible below 2 TeV, but become important with increasing energy.

Electromagnetic interactions

The main interaction processes for electromagnetic shower are Compton scattering, bremsstrahlung and pair production.

4.4.4 Čerenkov radiation

If the charged particle is moving through some medium with the velocity v , which is higher than the local speed of the light in given medium, the particle emit Čerenkov photons. So the primary condition for the origin of the Čerenkov radiation is:

$$v > \frac{c}{n}, \quad (4.8)$$

c is the speed of light in the vacuum and n is the index of refraction of given medium.

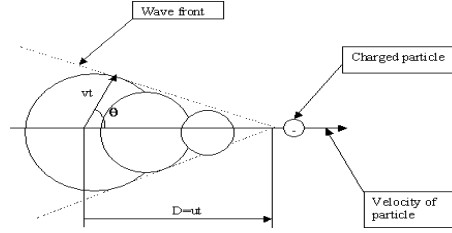


Figure 4.3: Illustrative picture of the Čerenkov radiation.

The Čerenkov photons are emitted in the angle Θ (see fig. 4.3). The value of this angle can be described by following formula:

$$\cos \Theta = \frac{1}{\beta n} \quad (4.9)$$

where $\beta = v/c$.

From the equation (4.9) we can determine the minimum velocity of the particle for emission of Čerenkov radiation. For the minimal velocity of the particle the condition is:

$$\beta_{min} = \frac{1}{n}. \quad (4.10)$$

The number of photons between the wavelengths λ_1 and λ_2 , which will be created at the distance l is equal to:

$$N(\lambda_1, \lambda_2) = \frac{2\pi Z^2}{137} l \left(\frac{1}{\lambda_1} - \frac{1}{\lambda_2} \right) \sin^2 \Theta. \quad (4.11)$$

where Z is the proton number of the particle.

4.4.5 Atmospheric fluorescence

The charged particle, which is moving through the atmosphere excites air molecules. The nitrogen molecules of the atmosphere is excited to the metastable energy levels. In very short time (≈ 100 ns) this electrons deexcite back to the ground state energy and they emit characteristic isotropic fluorescence light. The nitrogen fluorescence spectrum is shown in the figure (4.4).

By measuring the fluorescence the maximum and the energy of the showers can be measured.

In fig. (4.5) it can be seen, that Čerenkov radiation is strongly collimated in contrast with the isotropic fluorescence light.

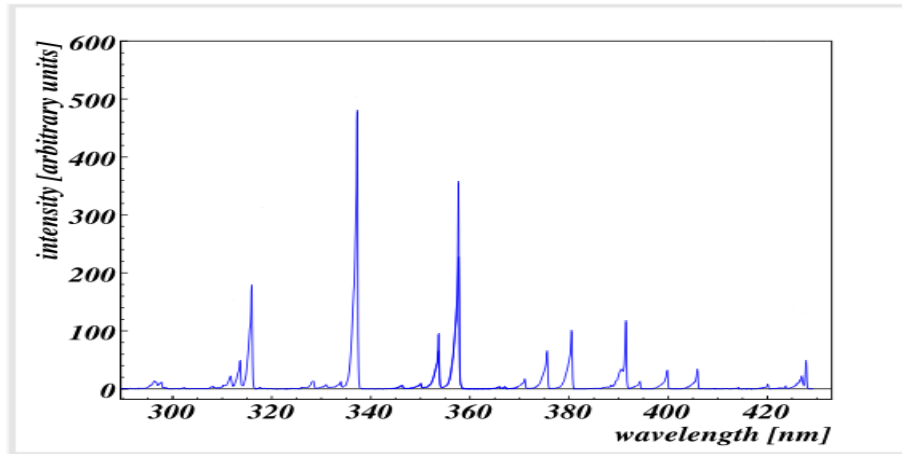


Figure 4.4: The most prominent part of the nitrogen fluorescence spectrum. This picture is taken from [19].

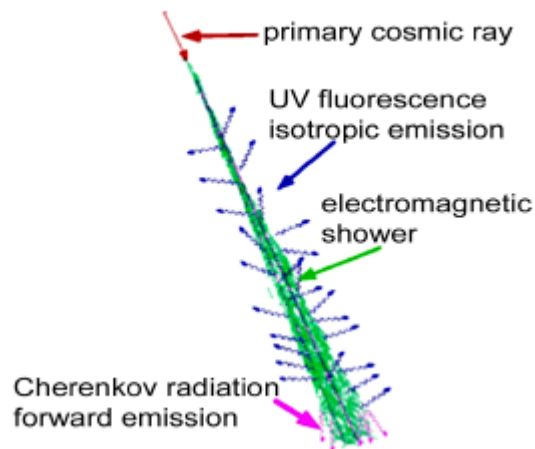


Figure 4.5: The comparison of the fluorescence and Čerenkov radiation. It can be clearly seen, that fluorescence is isotropic, while the Čerenkov radiation is strongly collimated. This picture is taken from [20].

4.4.6 The longitudinal development of the shower

The longitudinal development of the shower can be approximately described by the following formula [21]:

$$f_{GH}(X) = \frac{dE}{dX_{max}} \left(\frac{X - X_0}{X_{max} - X_0} \right)^{\frac{X_{max} - X_0}{\lambda}} e^{-\frac{X_{max} - X}{\lambda}} \quad (4.12)$$

where $\frac{dE}{dX_{max}}$ is energy deposit at shower maximum, X_0 is the point of the first interaction, X_{max} is the point of the shower maximum and λ is a constant (sometimes identified as an interaction length).

This equation (4.12) can be overwrite to another form:

$$N(X) = N_{max} \left(\frac{X - X_0}{X_{max} - X_0} \right)^{\frac{X_{max} - X_0}{\lambda}} e^{-\frac{X_{max} - X}{\lambda}} \quad (4.13)$$

where $N(X)$ is the number of the particles in the slant depth X and N_{max} is the number of the particles in the shower maximum.

4.4.7 The lateral profile

The lateral profile is usually described as particle density as a function of distance to the shower core.

The lateral distribution function

From the electromagnetic cascade theory it can be shown, that an average shower will have a particle density dependence on perpendicular distance from the shower axis given by [1]:

$$\rho(r) = \frac{N}{r_1^2} f\left(s, \frac{r}{r_1}\right), \quad (4.14)$$

where N is the total number of electrons, r_1 is the Moliere multiple scattering unit and s is the age of the electromagnetic shower. The shower age is defined as [1]:

$$s = \frac{3}{2y/t}, \quad (4.15)$$

where t is the distance along the shower in radiation lengths and

$$y = \ln \frac{E_0}{E_c},$$

where E_0 is incident energy and E_c is critical energy.

The function f was calculated from electromagnetic cascade theory by Nishimura and Kamata [22] and can be represented by:

$$f\left(s, \frac{r}{r_1}\right) = \left(\frac{r}{r_1}\right)^{s-2} \left(1 + \frac{r}{r_1}\right)^{s-4.5} \Gamma(4.5 - s) / [2\pi\Gamma(s)\Gamma(4.5 - 2s)]. \quad (4.16)$$

For hadronic showers, the experimental average lateral distribution function can be well represented by the Nishimura-Kamata equation with effective age of 1.25. The full function ($\rho(r)$) is then known as the NKG (Nishimura-Kamata-Greisen) lateral distribution function.

The lateral distribution of muons

The lateral distribution function of muons is described by the following formula [2]:

$$\rho_{\mu}(r) = 18 \cdot \left(\frac{N_e}{10^6} \right)^{0.75} + \left(1 + \frac{r}{320} \right) \text{ [muons/m}^2\text{]}, \quad (4.17)$$

where r is a distance to the core in a meters, N_e is the total number of charged particles in the shower front, most of them are electrons and positrons.

Chapter 5

The Measurement Techniques of UHECR

In this chapter the basic principles of the measurement techniques and procedures how to obtain primary particle energy, direction and other shower characteristics will be described. The aim is not to explain in details various experiments but rather to concentrate on a specific example of new and world largest cosmic ray detector Pierre Auger Observatory currently built and operated in Argentina. The techniques of surface array and fluorescence detector of Pierre Auger Observatory cover in basic principles the measurement techniques used by previous experiments HIRES (fluorescence detector) and AGASA (surface array). The only significant difference is that the measurement of fluorescence detectors (FD) is used here to calibrate the energy of the showers while the data taken by surface detectors (SD) is used to enlarge significantly the statistics for many analysis such as e.g. the energy spectrum.

5.1 The Pierre Auger Observatory

The Pierre Auger Observatory (PAO) is an international project for detection of high energy cosmic rays. It is the biggest project for the detection of CRs in the world. This project takes name after French scientist Pierre Auger, who discovered the secondary showers of CR in the year 1938. PAO is a collaboration of more then 30 institutes from 17 countries. More than 350 scientists participate in the experiment.

The basic idea of observatory comes from prof. James Cronin (he was awarded the Noble prize in 1980) from the Univesrity of Chicago and prof. Alan Watson from the University of Leeds. The international collaboration on this project began in November 1995. The main goal of PAO is the detection of cosmic ray particles with energy higher than 10^{18} eV [39], [40].

PAO is build on the southern hemisphere. It is located in the pampa close to the city Malargüe in the province Mendoza in the West Argentina (see fig. 5.1). The works began in the year 2001 and this year (2008) the work will be finished. There is a plan to build a similar observatory in the northern hemisphere in the future.



(a) Location in Argentina



(b) Central building

Figure 5.1: The Pierre Auger Observatory - location and central building.

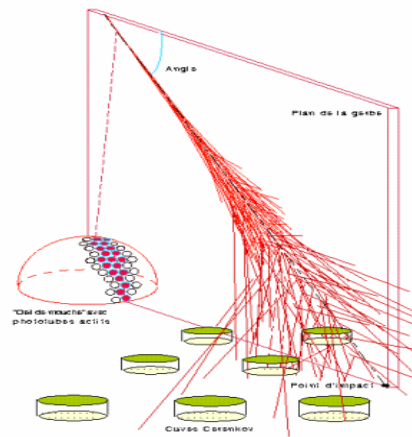


Figure 5.2: The scheme of hybrid detection.

PAO is a hybrid detector. This means, that PAO uses two different detections techniques to measure CRs. The first one is surface detector method and the second one is the fluorescence detector method. The combination of two measurements (see fig. 5.2) brings an independent calibration, better angular and energy resolution. The two detection techniques will be described separately now.

5.1.1 The surface detectors

Due to the extremely low flux of CRs particles with the highest energies the big area must be covered for such detection.

The surface detectors of PAO covers an area of about 3 000 km². Each detector is 1.5 km apart from another one. The final array will count 1 600 surface detectors (see fig. 5.3).

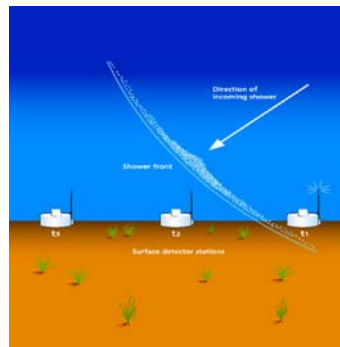


Figure 5.3: The final scheme of all surface detectors (blue points) used at PAO in Argentina. The yellow labels represent the places, where are the fluorescence telescopes placed.

The Čerenkov detectors are used as surface detectors at PAO. It is a plastic tank (see fig. 5.4(a)), which is filled with 12 000 liters of clean water. Each detector has three photomultipliers, solar panel, electronics, communication antenna and GPS antenna.



(a) The Čerenkov detector, which is used at PAO.



(b) The time series of the signal from the detectors.

Figure 5.4: The surface detector at PAO.

From time series of the signals from the detectors (see fig. 5.4(b)) the arrival angle of the incoming shower can be determined. From the measured particle density the

energy of the shower can be calculated. From the number of muons and from the shape of the signal the estimation of the primary particle mass can be in principal done.

The big advantage of the SD is that these detectors are able to measure all the time. Disadvantage is the fact, that these detectors see only a 2D projection of the shower at the point it hits the Earth.

5.1.2 The fluorescence detectors

As it was mentioned above, PAO is a hybrid detector. The second measurement technique used is the atmospheric fluorescence detection.

The atmospheric fluorescence detectors (FD) are placed at four observatories (see fig. 5.5). Each observatory consists of six telescopes. The telescope has its own independent bay at the observatory. In front of telescopes, there is a filter, which transmits the light with wavelength between 300 - 400 nm only. Each telescope consists of mirrors (see fig. 5.6). The mirrors at each telescope make a collecting area of $3.6 \times 3.6 \text{ m}^2$. The camera is in the focus of each telescope and it is made from 440 photomultipliers. The viewing field is $30^\circ \times 30^\circ$. The telescopes can see the shower light from the distance up to 35 km.



Figure 5.5: One of the four observatories with atmospheric fluorescence detectors.

The big advantage is that the FD see almost the whole shower. So the development of the shower can be measured and studied. On contrary with SD can measure only during moonless night.

The fluorescence profile (see fig. 5.7) copies the distribution of the number of particles in the shower (respectively the energy deposit of the shower in the atmosphere). So by measuring the fluorescence profile the information about maximum of the shower and primary particle energy can be obtained.

To reconstruct the shower, the following steps must be done. At first, the background radiation (mainly Čerenkov radiation) must be subtracted. Then the measured signal must be converted to the energy deposit. After that the shower profile can be fit by



(a) Experimental set up.

(b) The detailed view.

Figure 5.6: The atmospheric fluorescence detectors used at PAO.

the Gaisser-Hillas function (4.12). From this fit, the maximum of the shower can be determined. As will be shown in the 8th chapter, the shower maximum is connected to the type of the primary particle. By the integration of this fit, the primary particle energy can be calculated.

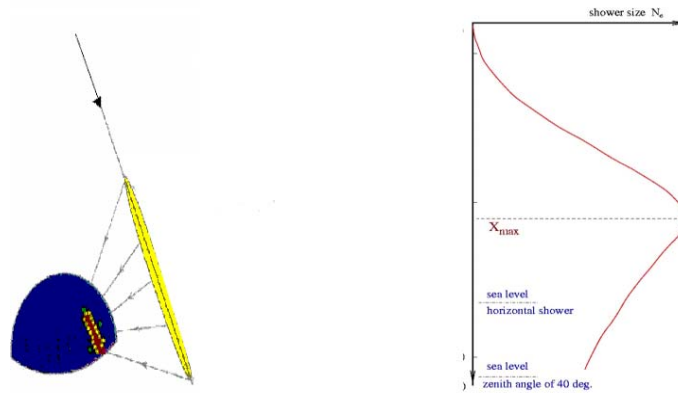


Figure 5.7: Measurement of the shower development by the FD.

Chapter 6

The Simulation Programs and Models

In this chapter the programs for simulation of cosmic air shower will be described. The interactions models, which are currently used will be introduced. The simulations of the atmospheric showers of secondary CRs are very important for our understanding of measured data. Ways, how this showers can be simulated, will be described.

The straightforward approach is to model each possible interaction of hadrons, leptons and photons with air molecules, and trace all secondary particles [23]. The number of possible interactions quickly increase with the growing numbers of secondary particles. So the simulation time of one shower caused by the particle with the ultra-high primary energy would take months. This is a big disadvantage of this approach.

One of the first people, who tried to solve this problem was Hillas. He proposed a thinning algorithm. Below some fraction f_{thin} of the primary particle energy only a small sample of the particles is actually followed in details, attributing them some weight [23]. But this solution brings an artificial fluctuations and the compromise between size of these fluctuations and computation time must be chosen.

The way, how to overcome this problems (long computation time, fluctuations) is to use **cascade equations**. The system of cascade equations (mostly one-dimensional) describes air showers. These equations can be then combined with Monte-Carlo in order to account for natural fluctuations due to the first interactions and for lateral spread [23] (for the scheme see fig. 6.1). This is the principle of the **hybrid approach**. The hybrid approach can be also combined with shower libraries, which contain presimulated longitudinal profiles.

6.1 The simulations programs

6.1.1 CORSIKA

CORSIKA is a simulation program for detailed simulation of the showers of CR originally designed for KASCADE experiment. Protons, nuclei up to the iron, photons

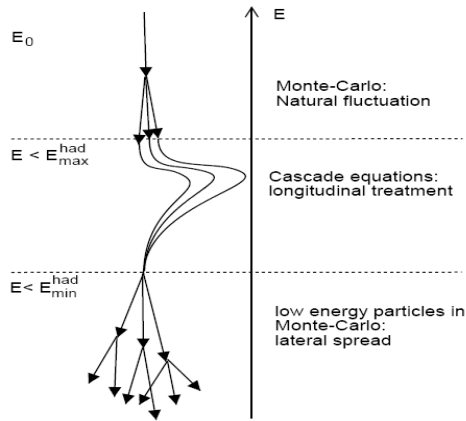


Figure 6.1: Schematic illustration of the hybrid approach using cascade equations in SENECA [23].

and many other particles may be treated as primaries [18]. The particles are traced through the atmosphere until they interact or decay. All decay modes are taken into account, if the decay fraction is higher than 1%. Also the Čerenkov radiation and neutrinos can be generated.

In CORSIKA, these high-energetic interaction models can be used: VENUS [24], QGSJET [25], QGSJETII, DPMJET [26], Sybill [27], Epos [28] and neXus [29]. The low-energetic interaction models are GHEISHA [30], ISOBAR or FLUKA [31].

CORSIKA was not used in this work, because only the longitudinal profile of the shower was needed for our purposes.

6.1.2 CONEX

CONEX is a hybrid simulation code, that is suited for fast one-dimensional simulations of showers profiles, including fluctuations. That means, that CONEX combines Monte Carlo (MC) simulation for high energy interactions with fast numerical solution of cascade equations (CE) for the resulting distributions of secondary particles.

The main input parameters are the mass of primary particle, its energy, zenith angle and high energy interaction model. The energy deposit profile as well as charged and muon longitudinal profiles are calculated. The results from the simulation are stored in the ROOT files.

In CONEX, these high-energetic interaction models can be used: neXus, QGSJET, Sibyll, QGSJETII.

6.1.3 SENECA

SENECA is an air shower simulations code in a hybrid approach using a cascade equations. See (fig. 6.1) for schematic illustration.

The SENECA simulation code allows the fast simulation, where the main parameters are the type of the primary particle, the energy of the primary particle and the number of showers. The results from the simulation are stored in a common text files.

In SENECA, these high-energetic interaction models can be used: QGSJET, Sybill, QGSJET II, Epos and nEXus.

6.2 The interactions models

The interaction models will be not discussed in details. Only general characteristics of these models will be shown such as cross sections, multiplicity distributions, muon energy spectra etc.

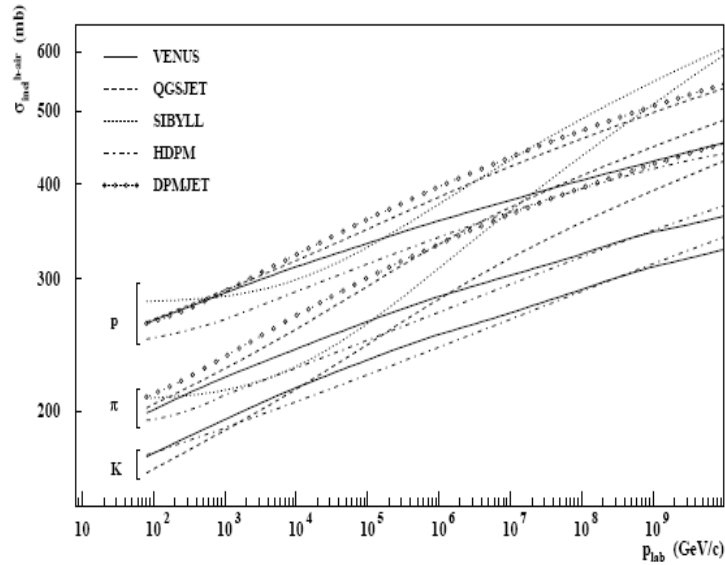


Figure 6.2: Inelastic hadron-air cross sections at higher energies of various interaction models. This picture was taken from [18].

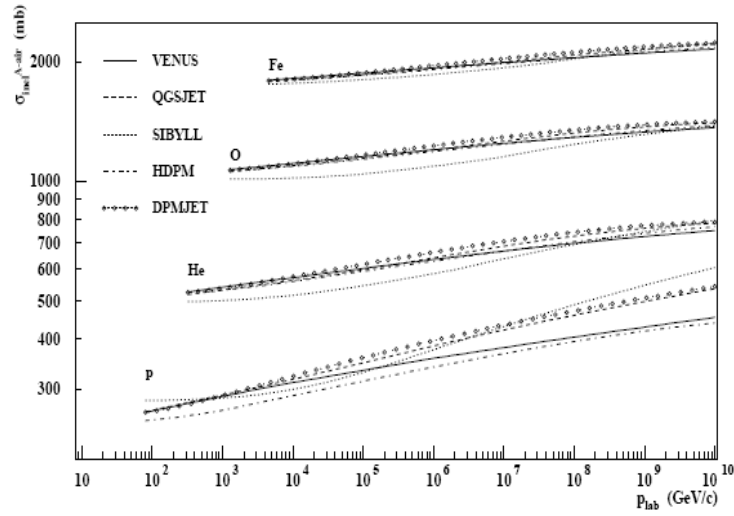


Figure 6.3: Inelastic nucleus-air cross sections of various projectile nuclei for the interaction models as function of projectile momentum. This picture was taken from [18].

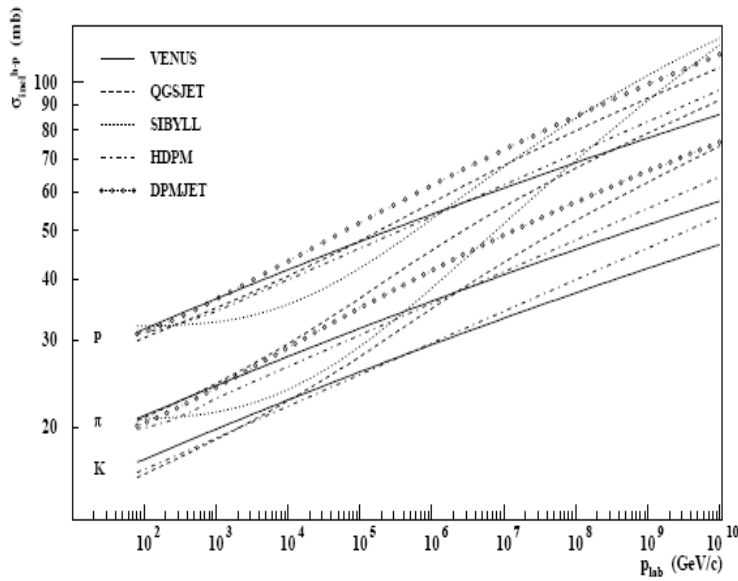


Figure 6.4: Inelastic cross sections of protons, pions, and kaons with protons for different interaction models as function of projectile momentum. This picture was taken from [18].

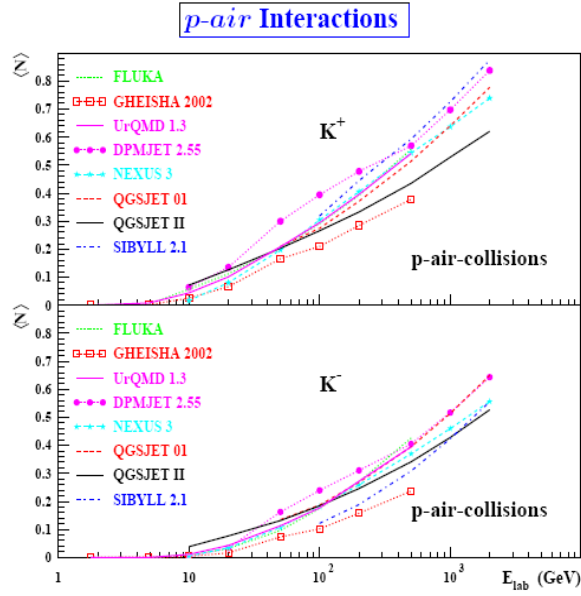


Figure 6.5: K^\pm multiplicities in proton-air collisions as function of energy. This picture was taken from [18].

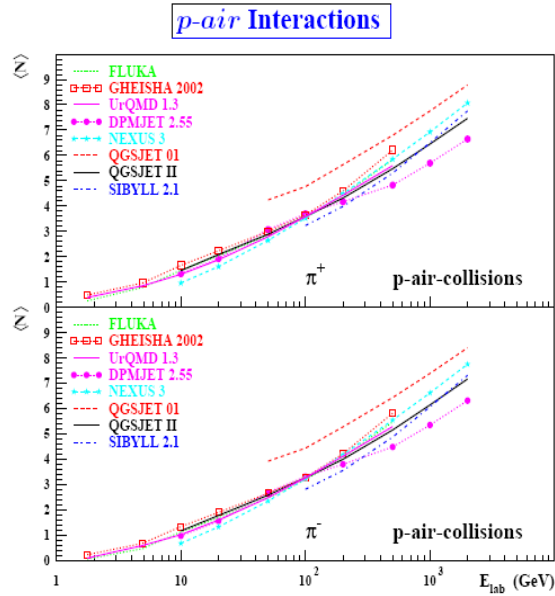


Figure 6.6: π^\pm multiplicities in proton-air collisions as function of energy. This picture was taken from [18].

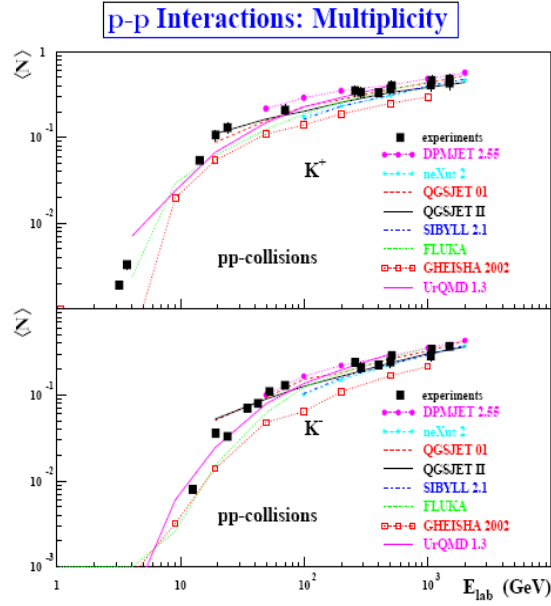


Figure 6.7: K^\pm multiplicities in pp-collisions as function of energy. This picture was taken from [18].

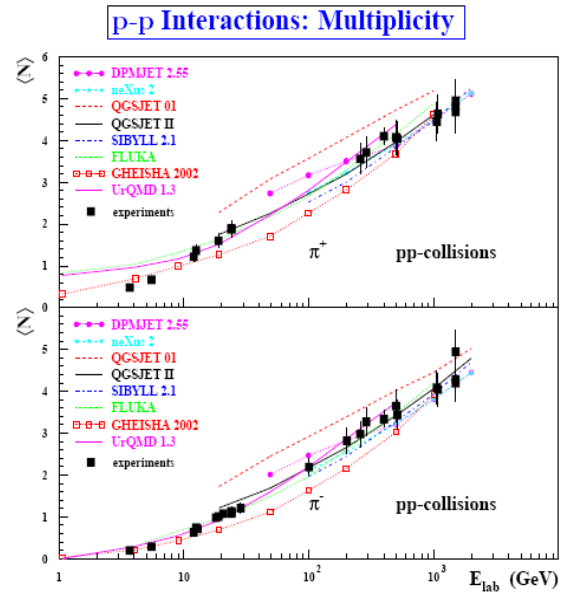


Figure 6.8: π^\pm multiplicities in pp-collisions as function of energy. This picture was taken from [18].

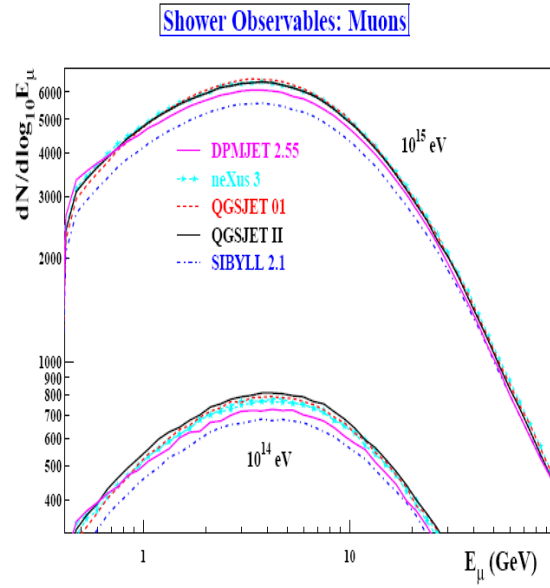


Figure 6.9: Muon energy spectra for iron induced vertical showers of 10^{14} and 10^{15} eV. This picture was taken from [18].

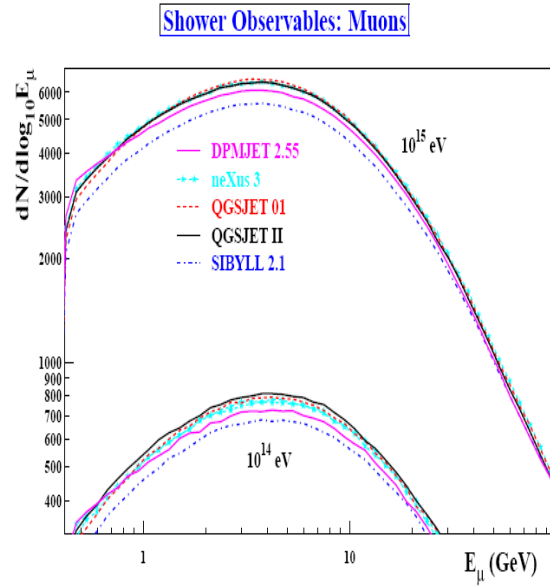


Figure 6.10: Muon energy spectra for proton induced vertical showers of 10^{14} and 10^{15} eV. This picture was taken from [18].

In the figures (6.2), (6.3) and (6.4) there are cross sections for different interaction processes given by various interaction models. Generally for all these interactions it can be said, that the cross section is increasing with increasing energy. In the case of hadron-air interaction (see fig. 6.2), the highest value of cross section is given by SYBILL interaction model and at the highest energies also by neXus. The QGSJET01 and QGSJET02 give the similar values in the case of protons and kaons. In the case of pions, QGSJET01 gives a higher value than QGSJET02. In the case of nucleus-air interaction (see fig. 6.3) for proton, the spread of cross section values given by different interaction models becomes more wide with increasing energy. In other cases, the interaction models give similar values.

In the figures (6.5) and (6.6) the multiplicity of kaons and pions is shown. The multiplicity becomes higher with increasing energy. In the case of kaon multiplicity, the low energy interaction model GHEISHA2002 gives the smallest value. QGSJET01 and QGSJET02 give the similar values at the lower energy range, but at the highest energies, QGSJET01 gives higher values. SYBILL gives the lowest value (except of GHEISHA) in the case of K^- but at the highest energies gives a little bit higher value than QGSJET02. In the case of K^+ SYBILL gives higher value than QGSJET01 and QGSJET02. In the case of pion multiplicity, the highest values are given by QGSJET01.

The kaon and pion multiplicities for proton-proton collisions are shown in the figures (6.7) and (6.8). In both cases (kaons and pions) multiplicity is increasing with increasing energy. The lowest values in both cases are given by GHEISHA2002 (this model is currently used as a low energy interaction model). In the case of kaons, QGSJET01 and QGSJET02 are in a good agreement with the experimental data from various experiments. NeXus and SYBILL give a little bit lower values than QGSJET01 and QGSJET02. QGSJET01 gives the highest values in the case of pions. QGSJET02 and neXus are in a good agreement with the experimental data. SYBILL gives a little bit lower values.

The muon energy spectra are shown in the figures (6.9) and (6.10). In the case of proton induced shower (for both primary energies) SYBILL gives the lowest values and QGSJET01, QGSJET02 and neXus give similar values. In the case of iron nucleus induced shower QGSJET02 gives the highest values, QGSJET01 and neXus give lower values and the lowest values are given by SYBILL.

Chapter 7

The Determination of the Chemical Composition

In this chapter the two models, how to determine the chemical composition will be described.

7.1 The elongation rate

The change of $\langle X_{max} \rangle$ (see section 4.4.6) with energy is so called elongation rate. From the elongation rate the estimation of the primary composition can be done.

The average value of X_{max} at a certain energy E is related to the mean logarithmic mass $\langle \ln A \rangle$ by [11]:

$$\langle X_{max} \rangle = D_p [\ln(E/E_0) - \langle \ln A \rangle] + c_p, \quad (7.1)$$

where D_p denotes the elongation rate of a proton and c_p is the average $\langle X_{max} \rangle$ of a proton with reference energy E_0

7.2 Two component model

In this section we will assume, that there are only two components in CR - protons and iron nuclei. This simplification comes from the fact, that protons are the lightest particles and iron nuclei are the heaviest particles appearing in CR.

The mean value of the shower maximum X_{max} can be written as the following equation:

$$\langle X_{max} \rangle = \frac{\sum_{i=1}^N X_{max}}{N}, \quad (7.2)$$

where N is a number of all X_{max} values (measured or simulated).

In the case of two components the mean value of X_{max} can be written as follows:

$$\langle X_{max} \rangle = p \cdot \frac{\sum_{i=1}^{Np} X_{max}^p}{Np} + (1-p) \cdot \frac{\sum_{i=1}^{N(1-p)} X_{max}^{Fe}}{N(1-p)}, \quad (7.3)$$

where X_{max}^p is for protons, X_{max}^{Fe} is for iron nuclei, p is a fraction of protons and N is number of all X_{max} values.

Using the equation (7.3) we can obtain following equation:

$$\langle X_{max}^{data} \rangle = p \cdot \langle X_{max}^p \rangle + (1-p) \cdot \langle X_{max}^{Fe} \rangle. \quad (7.4)$$

For two component model we finally end up with:

$$p = \frac{\langle X_{max}^{data} \rangle - \langle X_{max}^{Fe} \rangle}{\langle X_{max}^p \rangle - \langle X_{max}^{Fe} \rangle}, \quad (7.5)$$

where p is a fraction of protons⁽¹⁾, $\langle X_{max}^{data} \rangle$ is the mean value of the shower maximum of measured data, $\langle X_{max}^p \rangle$ ($\langle X_{max}^{Fe} \rangle$) is the mean value of the shower maximum for protons (iron nuclei) which can be taken from simulations.

7.3 Mean logarithmic mass

In this model, there is a basic assumption, that $\langle X_{max} \rangle$ of component i is proportional to $\ln A_i$ (see eq. 7.1):

$$\langle X_{max}^i \rangle \approx \ln A_i + C.$$

Let us define the mean logarithmic mass $\langle \ln A \rangle$, where A is a atomic number, r_i is a fraction of component i and N is a number of components:

$$\langle \ln A \rangle = \sum_{i=1}^N r_i \ln A_i. \quad (7.6)$$

In the case of two components (protons and iron nuclei) we can rewrite this equation to the following form⁽²⁾:

$$\langle \ln A \rangle = (1-p) \ln A_{Fe}, \quad (7.7)$$

where $1-p$ is iron nuclei fraction and $\ln A_{Fe}$ is logarithm of atomic number of iron ($A = 56$).

If we use the equations (7.5) and (7.7) we obtain the final equation for two component model:

$$\langle \ln A \rangle = \frac{\langle X_{max}^p \rangle - \langle X_{max}^{data} \rangle}{\langle X_{max}^p \rangle - \langle X_{max}^{Fe} \rangle} \ln 56, \quad (7.8)$$

where $\langle X_{max}^{data} \rangle$ is the mean value of the shower maximum of measured data, $\langle X_{max}^p \rangle$ ($\langle X_{max}^{Fe} \rangle$) is the mean value of the shower maximum for protons (iron nuclei) obtained from simulations. It can be shown, that equation (7.8) holds generally, independently on the number of components.

¹The fractions of iron nuclei can be determined as $1 - p$.

²Because for protons $p \ln A = 0$.

Chapter 8

Results of Simulation in the SENECA Simulation Code

In this chapter the results of simulation with the SENECA simulation code will be described. The results of X_{max} are presented and influence of the interaction models to the estimation of the chemical composition, using the real data from PAO will be shown.

8.1 Results of simulation of X_{max}

In the table (8.1) the simulation set is given. For each model the number of showers, the minimum energy ($\log(E_{min})$) and the maximum energy ($\log(E_{max})$) of simulated showers are shown. The step in logarithm of energy was chosen to 0.5. In all cases, the model GHEISHA 2002 (low energy interaction model) was used.

model	particle	number of showers	$\log(E_{min})$	$\log(E_{max})$
EPOS	p	500	14	20
	Fe	100	14	20
SYBILL	p	100	14	20
	Fe	100	14	20
QGSJET01	p	100	14	20
	Fe	100	14	20
QGSJETII	p	100	14	19.5
	Fe	100	14	19.5

Table 8.1: The basic parameters of simulation in SENECA.

From this simulation, the value of X_{max} was obtained. This value was processed by C++ and ROOT and the results are shown in the following graphs (see fig. 8.1 and 8.2).

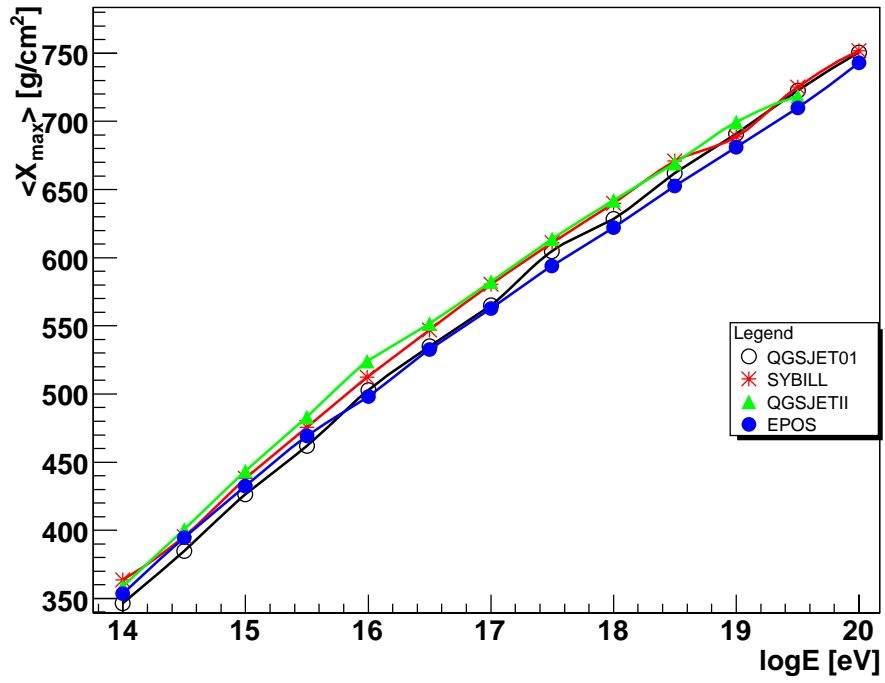


Figure 8.1: The comparison of mean X_{max} value obtained from different interaction models. The primary particle was iron nucleus. The symbols are explained in the legend panel. In all cases GHEISHA 2002 was used as the low energy interaction model.

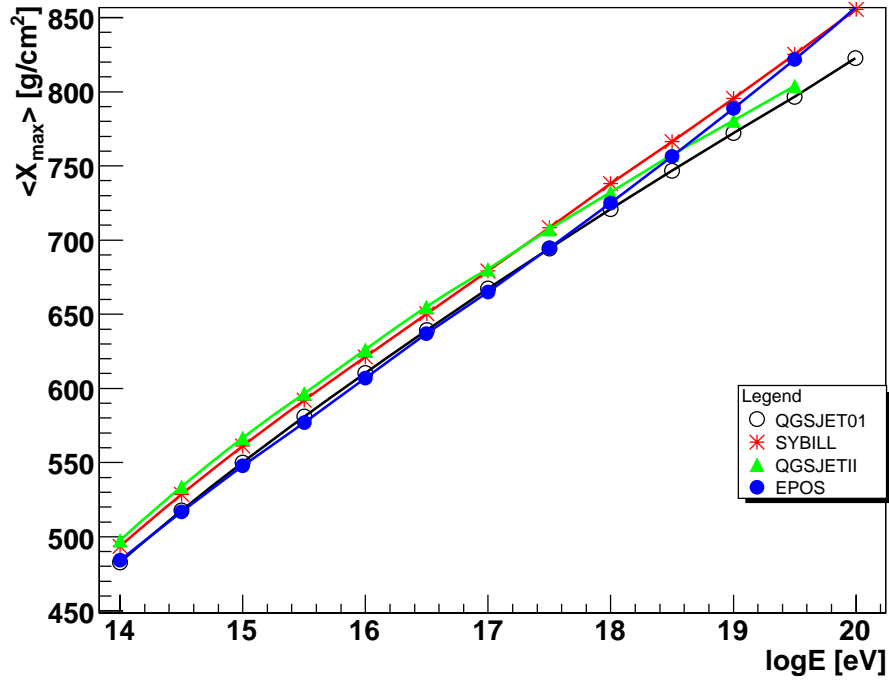


Figure 8.2: The comparison of X_{max} value obtained from different interaction models. The primary particle was proton. The symbols are explained in the legend panel. In all cases GHEISHA 2002 was used as the low energy interaction model.

In the case, that the primary particle was iron nucleus (see fig. 8.1), the biggest value of $\langle X_{max} \rangle$ is predicted by the high energy interaction model QGSJET02. The interaction model SYBILL gives value of $\langle X_{max} \rangle$ only a little bit lower than QGSJET02. At the highest simulated energy (10^{20} eV) SYBILL predicts the highest value of $\langle X_{max} \rangle$. The QGSJET01 interaction model predicts a little bit smaller value of $\langle X_{max} \rangle$ than QGSJET02 and SYBILL. But at the highest simulated energy $\langle X_{max} \rangle$ value of QGSJET01 is close to SYBILL. The smallest value of $\langle X_{max} \rangle$ is predicted by EPOS. At the highest simulated energy (10^{20} eV) the values of $\langle X_{max} \rangle$ predicted by different interaction models are close together in a good agreement (the spread of $\langle X_{max} \rangle$ values is quite small). This fact can be also clearly seen in the fig. (8.3).

Let us discuss the case, when the primary particle was proton (see fig. 8.2). Between the energies 10^{14} eV and 10^{18} eV QGSJET02 and SYBILL predict higher value of $\langle X_{max} \rangle$ than QGSJET01 and EPOS. Between the energies 10^{18} eV and 10^{19} eV SYBILL continuously predicts the highest value of $\langle X_{max} \rangle$ and QGSJET01 continuously predicts the lowest value of $\langle X_{max} \rangle$. But EPOS starts to predict a little bit higher value and becomes closer to SYBILL, while QGSJET02 starts to predict lower value of $\langle X_{max} \rangle$ and becomes closer to QGSJET01. Above the energies 10^{19} eV SYBILL and EPOS predict the highest $\langle X_{max} \rangle$, while the QGSJET01 and QGSJET02 predict the smaller values of $\langle X_{max} \rangle$. The spread of $\langle X_{max} \rangle$ values in the highest simulated energy predicted by different interaction models is higher than in the case of iron nuclei as primary particle (see also fig. 8.3).

In the table (8.2) the average values of $\langle X_{max} \rangle$ from all interaction models are shown together with maximum and minimum $\langle X_{max} \rangle$ values. These data are plotted in fig. (8.3). The influence of the interaction models to the $\langle X_{max} \rangle$ value is mostly between $8 \sim 12$ g/cm², but in the case of iron nuclei as primary particles with the simulated energy 10^{20} eV, the influence of the interaction models is only about $3 \sim 5$ g/cm². At the lower energy values, the influence of the interaction models is a little bit higher for iron nuclei, but at the highest simulated energies the influence of the model for iron nuclei is smaller than for protons.

$\log E$	avg_p	max_p	min_p	avg_{Fe}	max_{Fe}	min_{Fe}
14.0	489	498	482	356	364	346
14.5	524	534	517	394	400	383
15.0	556	567	548	435	444	426
15.5	587	597	577	472	483	462
16.0	616	626	607	509	523	498
16.5	645	655	636	542	552	533
17.0	673	681	665	573	583	563
17.5	701	708	693	606	614	594
18.0	729	737	721	633	624	644
18.5	757	767	747	664	671	653
19.0	784	795	772	690	699	681
19.5	812	825	797	719	725	709
20.0	845	857	822	748	745	754

Table 8.2: Table of average, maximum and minimum values of $\langle X_{max} \rangle$. $\log E$ is a logarithm of energy in eV, avg_p is the average $\langle X_{max} \rangle$ value for protons in the units of g/cm^2 , max_p is the maximum value of $\langle X_{max} \rangle$ for protons in g/cm^2 and min_p is minimum value of $\langle X_{max} \rangle$ for protons in g/cm^2 . Similarly avg_{Fe} is the average $\langle X_{max} \rangle$ value for iron nuclei in g/cm^2 , max_{Fe} is the maximum value of $\langle X_{max} \rangle$ for iron nuclei in g/cm^2 and min_{Fe} is minimum value of $\langle X_{max} \rangle$ for iron nuclei in g/cm^2 .

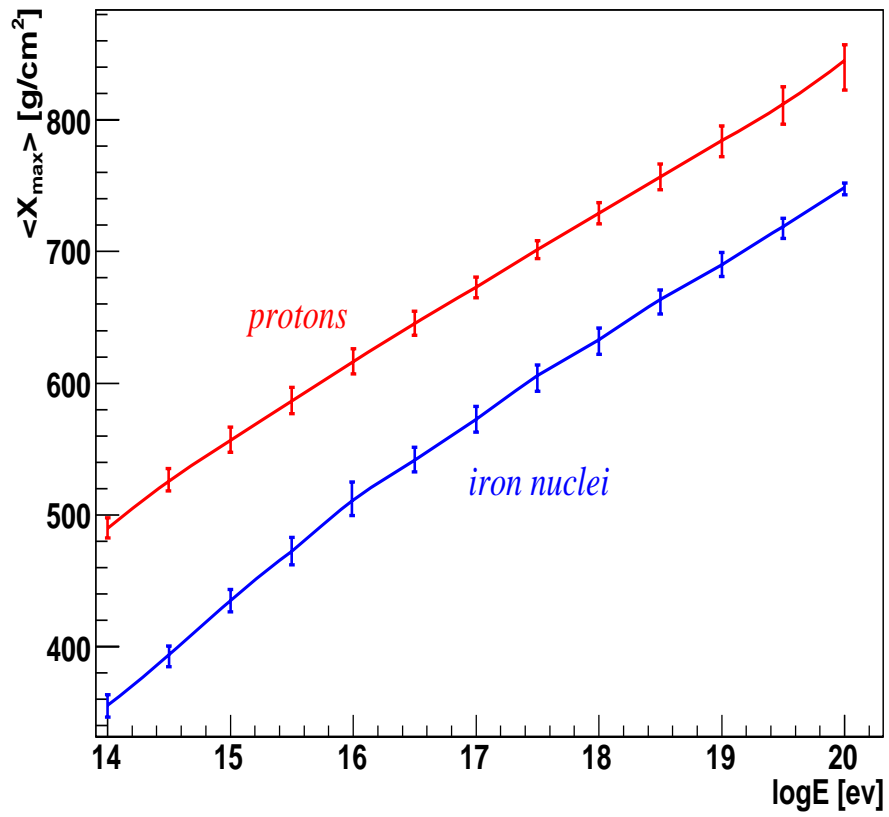


Figure 8.3: The value of $\langle X_{max} \rangle$ computed as average from all interaction models. The error bars represent value ranges and show the influence of the high energy interaction models.

8.2 The data measured by the Pierre Auger Observatory

The data, which were measured by Pierre Auger Observatory, were taken from [11]. These data together with the simulated data were used to determine the influence of the interaction models to the estimation of the chemical composition.

The data measured by PAO are shown in the figure (8.4) together with the simulated data.

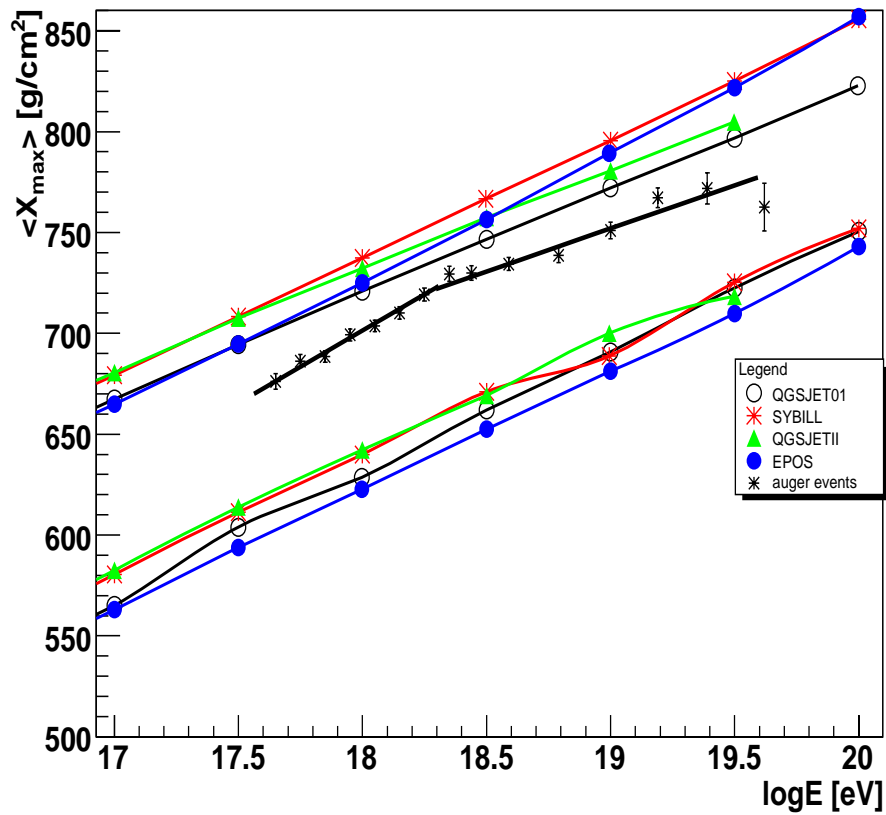


Figure 8.4: The data measured by PAO together with the data obtained from simulations.

8.3 The influence of high energy interaction models to the determination of chemical composition of cosmic rays

8.3.1 Results from individual models

To determine the chemical composition of CRs the methods described in the chapter (7.2) and (7.3) were used. The data obtained from the SENECA simulations and the data measured by PAO were used. The data from PAO are shown in the fig. (8.4). It seems from the data that there might be possible change of elongation rate (slope of the dependency $\langle X_{max} \rangle$ on E) at the energy $10^{18.35}$. To parameterize these data the two linear fits (below and above the energy $10^{18.35}$ eV) were done as suggested also in [11]. The equation (8.1) is for the fit below the energy $10^{18.35}$ eV and the equation (8.2) is for the fit above the energy $10^{18.35}$ eV.

$$y = 72.3x - 600.2 \quad (8.1)$$

$$y = 36.1x + 64.5 \quad (8.2)$$

For the two component model the fraction of protons was computed from the equation (7.5). The results are in the table (8.3) and they are plotted in the fig. (8.5). From the equation (7.8) the mean logarithmic mass was determined. The results are in the table (8.4) and they are plotted in the fig. (8.6).

	QGSJET01	QGSJET02	SYBILL	EPOS
$\log E$ [eV]	p [%]	p [%]	p [%]	p [%]
17.5	67.9	55.0	56.0	70.9
18.0	79.2	65.9	63.3	77.2
18.5	83.4	72.8	64.6	77.1
19.0	73.6	63.1	58.1	64.6
19.5	62.3	58.8	43.5	52.7
20.0	50.4	—	33.7	38.5

Table 8.3: The results of chemical composition computed from two component model (the two fractions are protons and iron nuclei). $\log E$ is a logarithm of energy and p [%] is a percentage fraction of protons. The fraction of iron nuclei is the rest.

log E [eV]	$\langle \ln A \rangle$			
	QGSJET01	QGSJET02	SYBILL	EPOS
17.5	1.3	1.8	1.8	1.2
18.0	0.8	1.4	1.5	0.9
18.5	0.7	1.1	1.4	0.9
19.0	1.1	1.5	1.7	1.5
19.5	1.5	1.7	2.3	1.9
20.0	2.0	—	2.7	2.5

Table 8.4: The values of the mean logarithmic mass. $\log E$ is a logarithm of energy, $\langle \ln A \rangle$ is the mean logarithmic of mass.

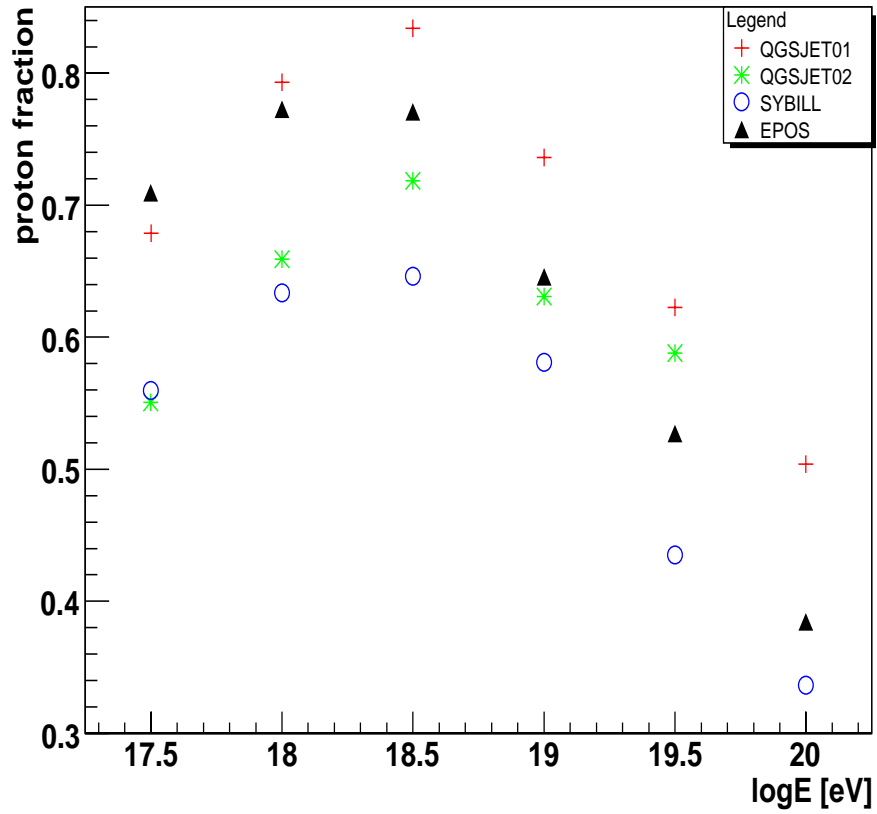


Figure 8.5: The results of chemical composition calculated from two component model for different interaction models. The symbols are explained in the legend panel.

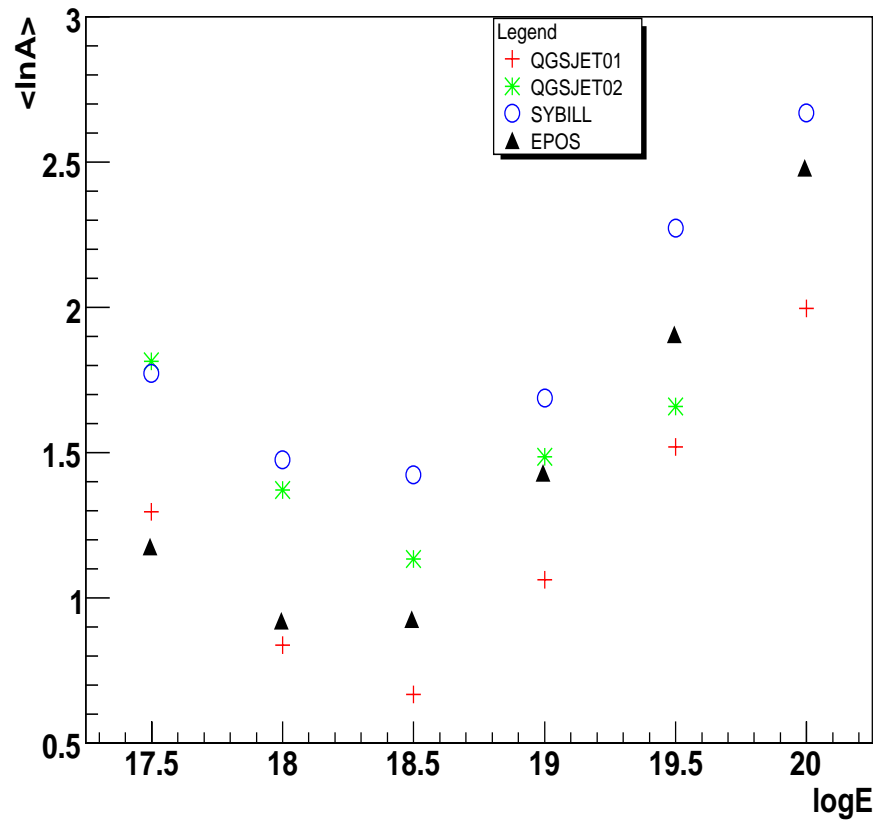


Figure 8.6: The mean logarithmic mass computed for different interaction models. The symbols are explained in the legend panel.

In fig. (8.5) the results of chemical composition computed from two component model are plotted. Generally it can be said, that all interaction models give at a lower range of energies increasing fraction of protons with increasing energy. The maximum of the proton fraction is approximately around the energy $10^{18.5}$ eV. Following with the increasing energy, the protons fraction is decreasing - the fraction of iron nuclei is increasing.

The most abundant proton fraction is predicted by the QGSJET01 interaction model (at the maximum gives the fraction of protons around 85%). On the other hand the EPOS interaction model gives the lowest proton fractions. At the highest simulated energies the fraction of iron nuclei is around 65 %.

In fig. (8.6) the results of mean logarithmic mass are plotted. This method gives more general results in the meaning, that the equation (7.8) holds generally independently on the number of components.

It can be said, that the mean logarithmic mass is decreasing between energy range $10^{17.5}$ eV to $10^{18.5}$ eV. Around the energy $10^{18.5}$ eV the mean logarithmic mass reaches the lowest values (the lightest nuclei are more abundant). Above this energy the value of mean logarithmic mass is increasing.

The lowest values of mean logarithmic mass are given by the QGSJET01 interaction model. On the other hand, the EPOS interaction model gives the highest values of mean logarithmic mass.

8.3.2 Model dependence

The influence of the interaction models to the estimation of chemical composition of CRs can be evaluated in two ways.

The first possibility is to determine the average value of $\langle X_{max} \rangle$ (for all interactions models) and then from this mean value determine the chemical composition and its model error.

The error is determine from following equation:

$$\sqrt{\left(\frac{\partial f}{\partial X_{max}^{Fe}}\right)^2 (\Delta_{X_{max}^{Fe}})^2 + \left(\frac{\partial f}{\partial X_{max}^p}\right)^2 (\Delta_{X_{max}^p})^2}, \quad (8.3)$$

where f is the function which represents the equation to determine the chemical composition, $\Delta_{X_{max}^{Fe}}$ is the error of mean value of $\langle X_{max}^{Fe} \rangle$ and $\Delta_{X_{max}^p}$ is the error of mean value of $\langle X_{max}^p \rangle$. For the set of simulation models the errors $\Delta_{X_{max}^{Fe}}$ and $\Delta_{X_{max}^p}$ are computed as maximum $\langle X_{max} \rangle$ value minus mean $\langle X_{max} \rangle$ value respectively as mean $\langle X_{max} \rangle$ value minus minimum $\langle X_{max} \rangle$ value. This represents a conservative assumption that the true $\langle X_{max} \rangle$ value can be wherever in the interval of obtained $\langle X_{max} \rangle$ values.

The second possibility is to determine chemical composition (fractions of protons or mean logarithmic mass) for each model separately and then determine the average value of these results and $\langle X_{max} \rangle$ value range. The value range is determined as maximum and minimum value of obtained proton fractions or mean logarithmic masses $\langle min, max \rangle$.

The influence of the models based on the average value of $\langle X_{max} \rangle$ obtained for different interaction models

The results of proton fractions determined from the average value of $\langle X_{max} \rangle$ are in the table (8.5). These results are plotted in fig. (8.7). The results of mean logarithmic mass determined from the average value of $\langle X_{max} \rangle$ are in the table (8.6) and they are plotted in fig. (8.8).

$\log E$	p [%]	er^+ [%]	er^- [%]
17.5	62.5	5.6	6.4
18.0	71.5	6.8	6.9
18.5	74.1	7.9	8.6
19.0	64.4	8.5	9.0
19.5	53.5	8.3	9.9
20.0	39.7	5.3	9.8

Table 8.5: The mean value of protons fraction computed from the average value of $\langle X_{max} \rangle$. $\log E$ is a logarithm of energy in eV, p is the protons fraction, er^+ is the plus error and er^- minus error.

$\log E$	$\langle \ln A \rangle$	er^+	er^-
17.5	1.5	0.2	0.3
18.0	1.2	0.3	0.3
18.5	1.0	0.3	0.4
19.0	1.4	0.3	0.4
19.5	1.9	0.3	0.4
20.0	2.4	0.2	0.4

Table 8.6: The mean logarithmic mass computed from the average value of $\langle X_{max} \rangle$. $\log E$ is a logarithm of energy in eV, $\langle \ln A \rangle$ is the mean logarithmic mass, er^+ is the plus error and er^- minus error.

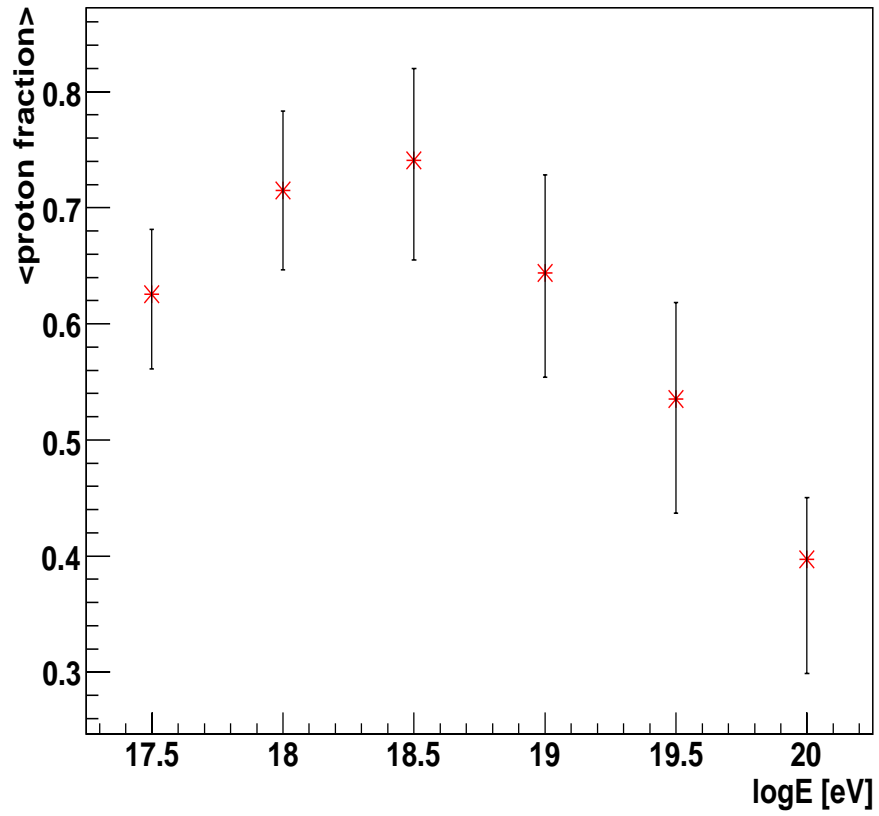


Figure 8.7: The mean value of proton fraction determined from the average value of $\langle X_{max} \rangle$ and corresponding errors, which represent the model dependence.

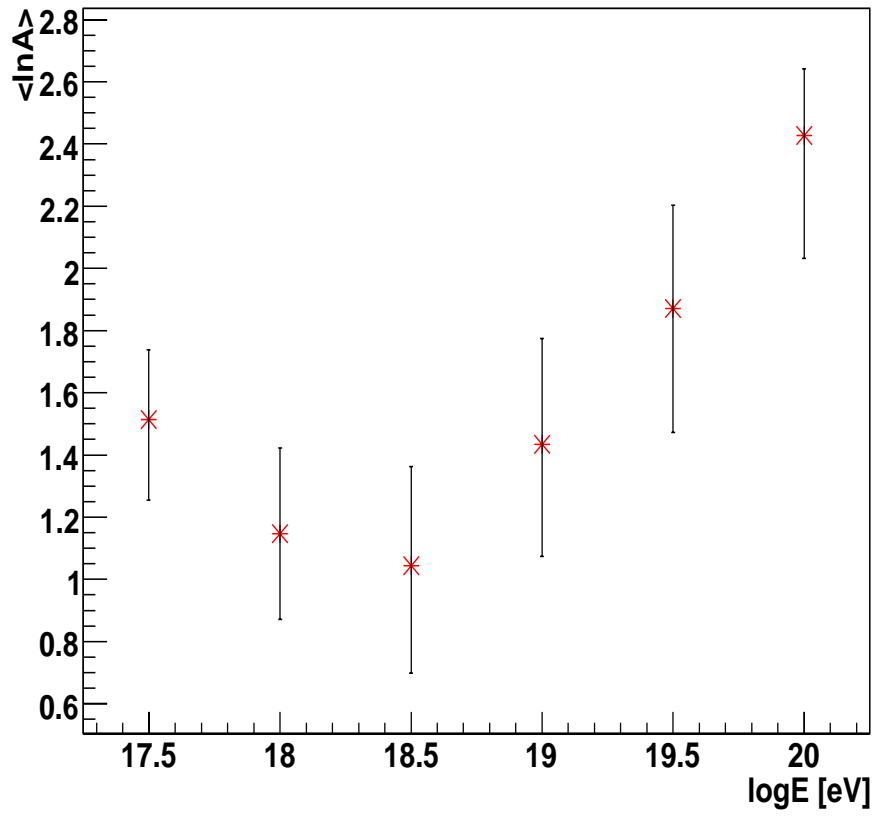


Figure 8.8: The mean logarithmic mass determined from the average value of $\langle X_{max} \rangle$ and corresponding errors, which represent the model dependence.

The results of proton fractions computed from the average values of simulated $\langle X_{max} \rangle$ are in the table (8.5). These results are plotted in fig. (8.7). Generally, the behavior of the proton fractions is similar as in the fig. (8.5) as it can be expected. At the lowest energy range, the proton fraction is increasing with increasing energy. The maximum of proton fraction is around the energy value $10^{18.5}$ eV. Above this energy, the proton fraction decreases. As can be clearly seen in the table (8.5), the uncertainty of the interaction models in determination of the proton fraction is between $\pm 5 \sim 10 \%$.

The results of mean logarithmic mass computed from the average values of simulated $\langle X_{max} \rangle$ are shown in the table (8.6). These results are plotted in fig. (8.8). Again, the behavior of mean logarithmic mass as a function of energy is similar as in fig. (8.6) as it can be expected. From the lowest energies the mean logarithmic mass value is decreasing with increasing energy (indicating that CRs are more abundant by the lighter nuclei). The minimum of the mean logarithmic mass (the most abundant light nuclei) is around the energy value $10^{18.5}$, this is in agreement with the two component model (the maximum of the proton fraction is around the same energy). In the table (8.6) also the errors of the mean logarithmic mass are shown. These errors represent the influence of the interaction models to the determination of the mean logarithmic mass. The influence of the interaction models is between $\pm 0.2 \sim 0.4$ of the value of $\ln A$.

The influence of the models based on the average value of chemical composition obtained from different interaction models

In the table (8.7) the results of proton fractions determined as the average of proton fractions from results of individual models are shown. These results are plotted in fig. (8.9). In the table (8.8) there are the results of mean logarithmic mass computed as average of mean logarithmic mass from different interaction models. These results are plotted in fig. (8.10).

$\log E$	p [%]	<i>max</i> [%]	<i>min</i> [%]
17.5	62.4	70.9	55.0
18.0	71.4	79.2	63.3
18.5	74.2	83.4	64.6
19.0	64.8	73.6	58.0
19.5	54.3	62.2	43.5
20.0	40.2	49.8	33.0

Table 8.7: The mean value of proton fraction determined as the average of proton fractions from each interaction model. $\log E$ is logarithm of energy, p is the proton fraction, *max* is the maximum value of proton fraction and *min* is the minimum value of proton fraction.

$\log E$	$\langle \ln A \rangle$	max	min
17.5	1.5	1.8	1.2
18.0	1.2	1.5	0.9
18.5	1.1	1.5	0.7
19.0	1.4	1.7	1.0
19.5	1.8	2.2	1.5
20.0	2.4	2.7	2.0

Table 8.8: The mean logarithmic mass determined as average of mean logarithmic masses from each interaction model. $\log E$ is logarithm of energy, $\ln A$ is mean logarithmic mass, max is the maximum value of the mean logarithmic mass and min is the minimum value of the mean logarithmic mass.

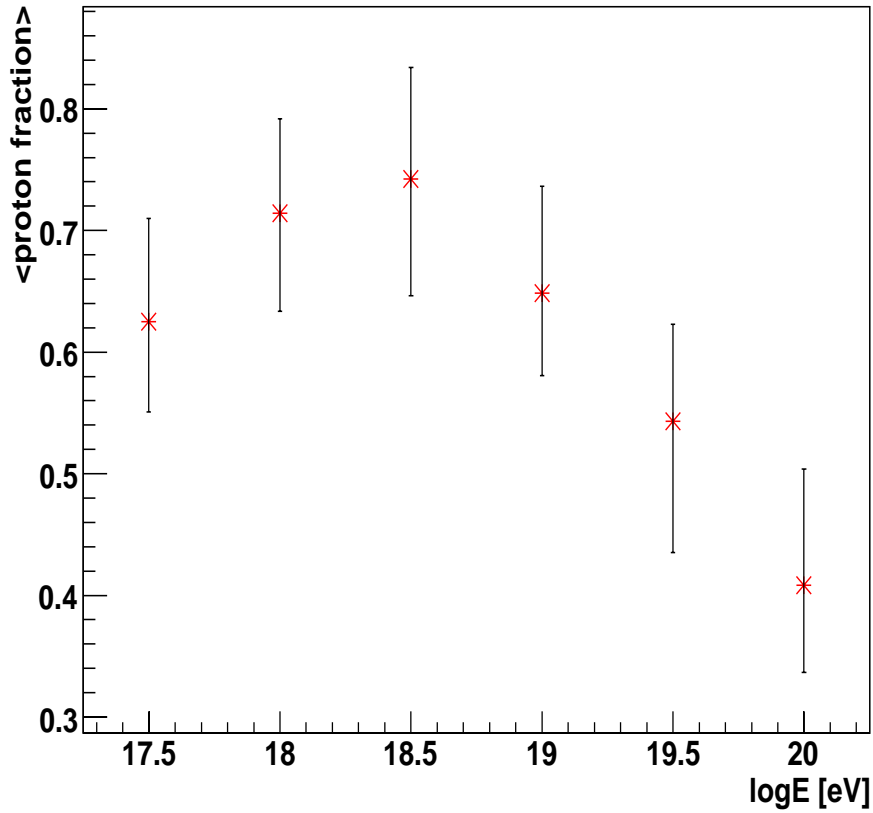


Figure 8.9: The mean value of proton fraction determined as average of the proton fractions from each interaction model and value ranges, which represent model dependence.

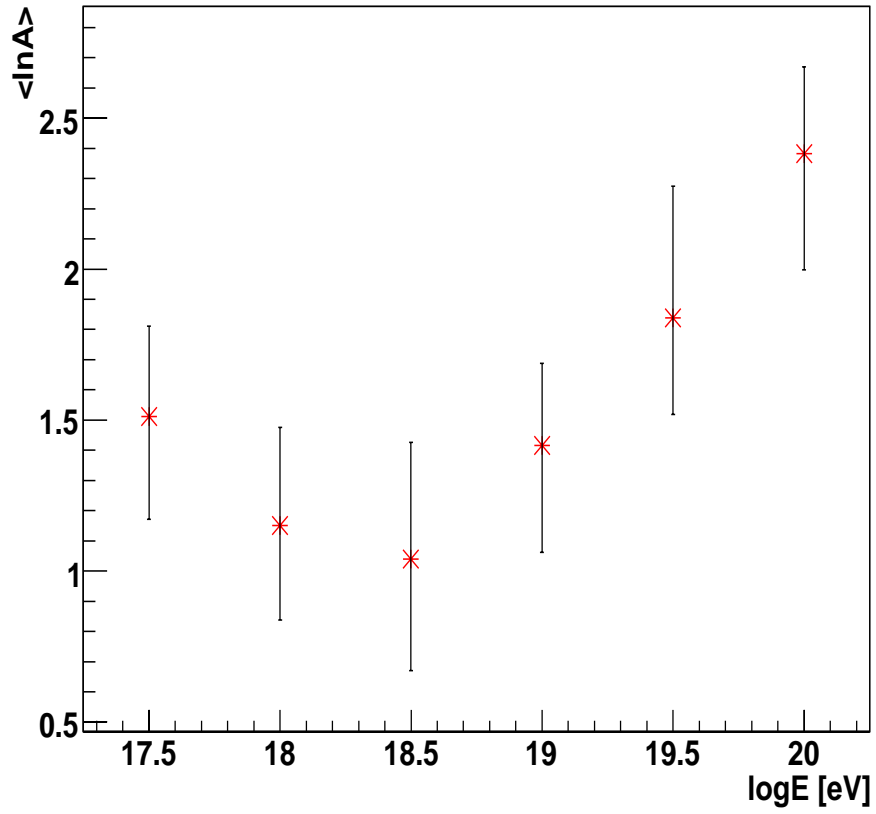


Figure 8.10: The mean logarithmic mass determined as average of the mean logarithmic mass from each interaction model and value ranges, which represent model dependence.

As can be clearly seen from the tables (8.7), (8.8) and figures (8.9), (8.10), the influence of the interaction models on the proton fraction is mostly between $\pm 7 \sim 10\%$. In the case of the mean logarithmic mass the influence of the interaction models is between $\pm 0.3 \sim 0.4$.

Remarks on the results

If we compare the results obtained by two ways (as average of $\langle X_{max} \rangle$ values and as average of the values of composition from separate models) we can make these conclusions:

1. Both ways of computing give almost the same values of chemical composition (proton fraction or mean logarithmic mass). The maximum difference in the case of proton fraction is 0.8% and in the case of mean logarithmic mass is the maximum difference 0.1.
2. The influence of the interaction models to the chemical composition of CRs is in the case of proton fraction mostly between $5 \sim 10\%$ and in the case of mean logarithmic mass mostly between $0.2 \sim 0.4$.
3. More frequently the influence of interaction models is a little bit higher in the case, that resulting chemical composition was determined as average of the chemical composition from separate models, but generally both methods give quite similar results concerning the error given by the choice of the interaction models.

Finally, these results of chemical composition are only rough estimates. Comparing with the last results of PAO (see the chapter 3.4 - *Anisotropy beyond 60 EeV*), CRs at the highest energies would be composed mostly from lightest nuclei. But results reported in this work show, that at the highest energies there is a significant fraction of heavy elements in CRs.

One of the possible explanations can be, that the parameters of interaction models (cross section, muon energy spectra, multiplicity distribution, etc.) are not known precisely enough. Because there are no accelerator data at such energies, these parameters are only extrapolated.

Hence confrontation between anisotropy studies and composition analysis such as the one presented here may address also the question to which extent we can believe model predictions.

Chapter 9

The Missing Energy

If the primary particle interacts in the Earth's atmosphere, the shower of secondary particles originates. The longitudinal development of the shower can be detected by fluorescence technique and the energy of primary particle can be then reconstructed. But some part of the primary energy⁽¹⁾ can not be detected, because a fraction of energy is carried away by neutrinos and due to the fact, that energy deposit of muons is very small. This part of primary energy is invisible to detectors and it is called **missing energy**.

9.1 The computation of the missing energy

One of the possible ways, how to determine the missing energy is to simulate longitudinal profiles and apply Gaisser-Hillas (GH) fit (see equation 4.12) to them. The calorimetric energy (E_{cal}), which can be detected by the detectors is then given by the integral of the energy deposit profile:

$$E_{cal} = \int_0^{\infty} f_{GH}(X) dX,$$

where f_{GH} is the GH function (see eq. 4.12) and X is the slant depth. Note that the integral is made to infinity in spite of the fact, that fluorescence detectors measure only part of the profile. The integral to infinity is because in this way the calorimetric energy is in fact estimated by the fluorescence experiments.

The above integral is then given by [32]:

$$E_{cal} = \lambda dE/dX_{max} \left(\frac{e\lambda}{X_{max} - X_0} \right)^{\frac{X_{max} - X_0}{\lambda}} \Gamma \left(\frac{X_{max} - X_0}{\lambda} + 1 \right), \quad (9.1)$$

where Γ denotes the gamma function.

Using the equations (4.12) and (9.1) one can obtain:

¹The energy of primary particle.

$$f_{GH} = \frac{E_{cal}}{\lambda} e^{\frac{X_0 - X}{\lambda}} \left(\frac{X - X_0}{\lambda} \right)^{\frac{X_{max} - X_0}{\lambda}} \Gamma \left(\frac{X_{max} - X_0}{\lambda} + 1 \right). \quad (9.2)$$

The missing energy (E_{miss}) can be then computed as:

$$E_{miss} = E_{prim} - E_{cal}, \quad (9.3)$$

where E_{prim} represents the primary particle energy.

9.2 The results of computation of the missing energy

All simulations for mean missing energy calculation were done in CONEX simulation code.

In the table (9.1) the set of simulations is given. The step in logarithm of energy was chosen to 0.5. In all cases zenith angle $\theta = 0^\circ$ was used.

model	particle	number of showers	$\log(E_{min})$	$\log(E_{max})$
neXus	p	500	17	20
	Fe	500	17	20
SYBILL	p	500	17	20
	Fe	500	17	20
QGSJET01	p	500	17	20
	Fe	500	17	20
QGSJETII	p	500	17	20
	Fe	500	17	20

Table 9.1: The basic parameters of simulations in CONEX. In all cases, the zenith angle $\theta = 0^\circ$ was used.

From the simulations in CONEX, the energy deposit (dE/dX) as a function of slant depth (X) can be obtained. These data can be directly used for fit by GH function (eq. 4.12) but in our case it is better to use equation (9.2). It is due to the fact, that in this formula E_{cal} is one of the parameters of the fit and it can be easily obtained from the fitting procedure.

If the parameter E_{cal} is obtained, the missing energy E_{miss} can be easily computed from the equation (9.3).

In fig. (9.1) one of the typical fits is shown. This plot is done for simulated data (interaction model - QGSJETII; primary particle - iron nucleus; primary energy - $10^{18.5}$ eV) and fit of equation (9.2).

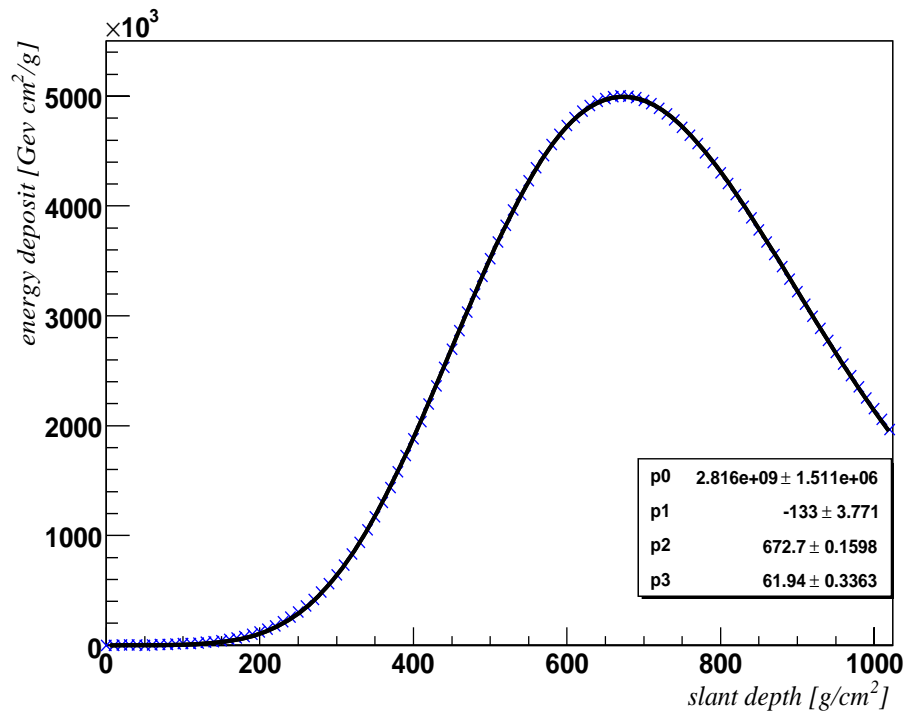
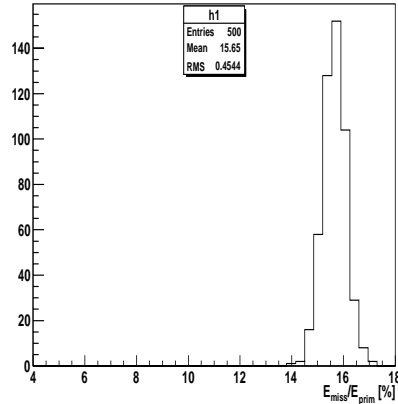


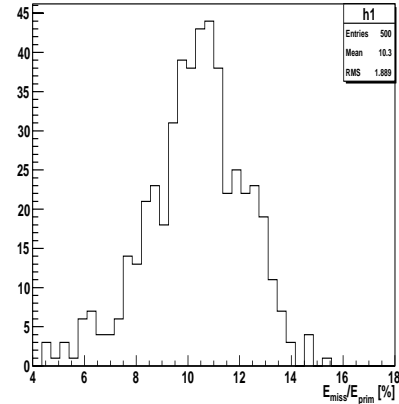
Figure 9.1: One of the typical fits. This fit was done for QGSJETII interaction model, the primary energy was $10^{18.5}$ eV and primary particle was iron nucleus. The fit of the equation (9.2) was made.

In the following figures (9.2) - (9.5) the distribution of the missing energy for different interaction models, primary particles and primary energies is shown.

From these figures one can clearly see, that the distribution of missing energy is wider in the case when primary particle was proton. That is due to shower fluctuations which are different for different primary particles. Iron shower can be very roughly approximated as 56 simultaneous proton showers at correspondingly lower energies. Hence the "averaging" of these subshowers makes the missing energy distributions less broad compared to proton primaries.

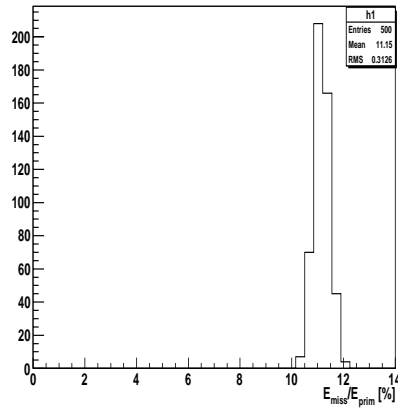


(a) neXus, iron nuclei, $E = 10^{17.5}$ eV.

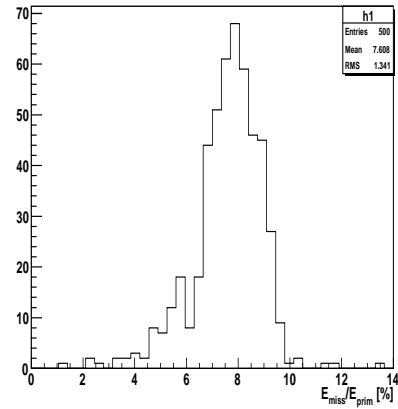


(b) neXus, protons, $E = 10^{17.5}$ eV.

Figure 9.2: The distribution of missing energy in %, neXus high energy interaction model.

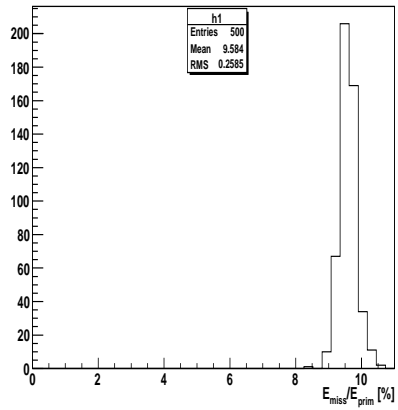


(a) QGSJTEII, iron nuclei, $E = 10^{18.5}$ eV.

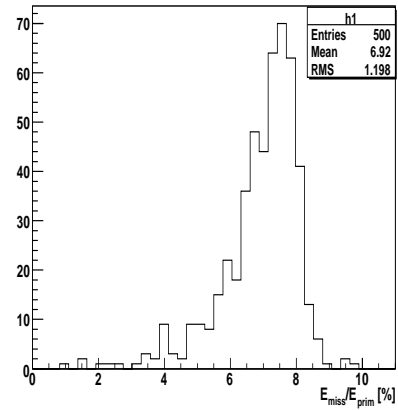


(b) QGSJTEII, protons, $E = 10^{18.5}$ eV.

Figure 9.3: The distribution of missing energy in %, QGSJET02 high energy interaction model.

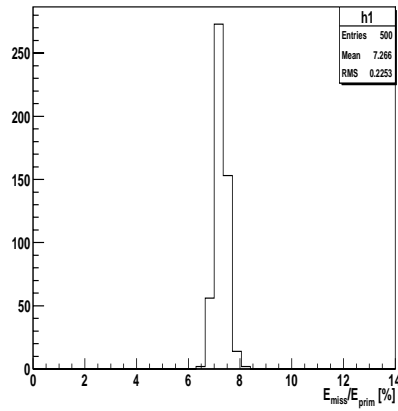


(a) QGSJTE01, iron nuclei, $E = 10^{19.5}$ eV.

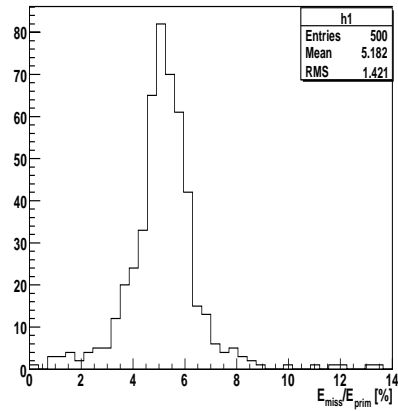


(b) QGSJTE01, protons, $E = 10^{19.5}$ eV.

Figure 9.4: The distribution of missing energy in %, QGSJET01 high energy interaction model.



(a) SYBILL, iron nuclei, $E = 10^{20.0}$ eV.



(b) SYBILL, protons, $E = 10^{20.0}$ eV.

Figure 9.5: The distribution of missing energy in %, SYBILL high energy interaction model.

The mean missing energy for a given high energy interaction model, primary particle and primary energy can be easily obtained by total sum of all values of missing energy divided by the number of simulated showers for given interaction model, particle and energy.

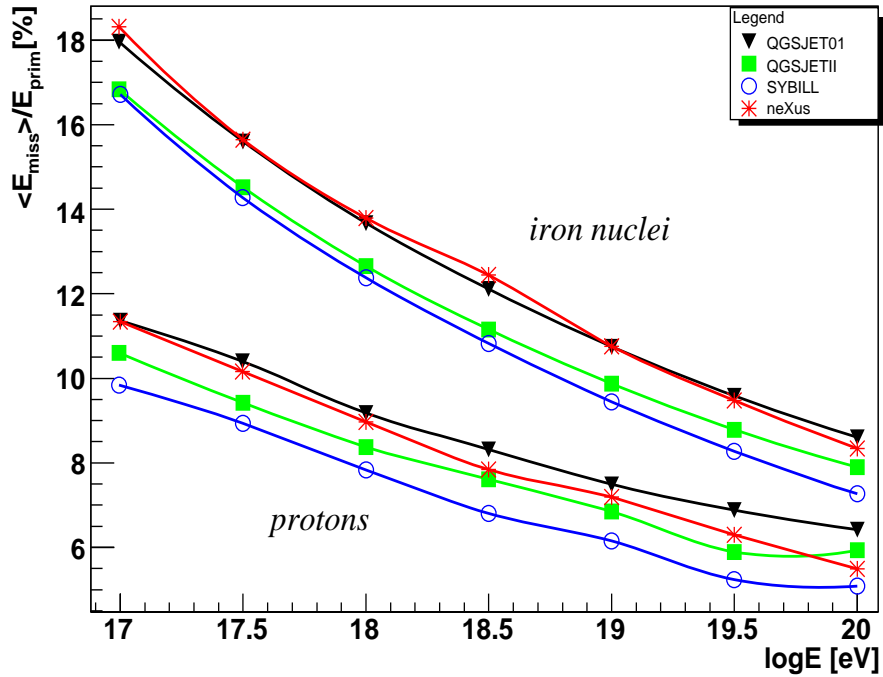


Figure 9.6: The mean missing energy as a fraction of primary energy (computed as an average from 500 simulated showers for each interaction model) for protons and iron nuclei as a function of energy. The QGSJET01, QGSJET02, SYBILL and neXus interaction model are used.

In the fig. (9.6) the mean missing energy as a function of energy for different high energy interaction models is plotted. One can see, that the mean missing energy is higher in the case of iron nuclei. It can be seen also, that in both cases (i.e. the primary particle is proton or iron nucleus) with increasing energy the fraction of mean missing energy is decreasing.

In both cases, SYBILL gives the lowest values of mean missing energy. QGSJET01 and neXus predict the highest values of mean missing energy. QGSJETII gives the value of mean missing energy smaller than QGSJET01 and neXus (exception is in the case of proton primary particle at the energy 10^{20} eV). QGSJETII also gives always higher values of mean missing energy than SYBILL interaction model.

The influence of chosen high energy interaction model on the missing energy

The influence of high energy interaction models on the mean missing energy can be simply determined. The average value of mean missing energies was calculated from all interaction models and maximum and minimum values represent the value range (the influence of the high energy interaction models on the mean missing energy).

In the tables (9.2) and (9.3) there are the results of average value of mean missing energy and the influence of interaction models for iron nuclei and protons. These results are plotted in fig. (9.7).

iron nuclei

$\log E$ [eV]	$\langle E_{miss} \rangle / E_{prim}$ [%]	max [%]	min [%]
17.0	17.4	18.2	16.7
17.5	15.0	15.7	14.3
18.0	13.1	13.8	12.4
18.5	11.6	12.5	10.8
19.0	10.2	10.8	9.5
19.5	9.0	9.6	8.3
20.0	8.0	8.5	7.3

Table 9.2: The average mean missing energy for iron nuclei as a function of energy and the influence of interaction models on the average mean missing energy. $\log E$ is logarithm of energy, $\langle E_{miss} \rangle / E_{prim}$ is the average mean missing energy in a percentage fraction of the primary energy, max is maximum value of the average mean missing energy and min is minimum value of the average mean missing energy.

protons

$\log E$ [eV]	$\langle E_{miss} \rangle / E_{prim}$ [%]	max [%]	min [%]
17.0	10.8	11.3	9.8
17.5	9.7	10.4	8.9
18.0	8.6	9.2	7.8
18.5	7.6	8.3	6.8
19.0	6.9	6.4	7.7
19.5	6.1	5.3	6.9
20.0	5.7	6.4	5.1

Table 9.3: The average mean missing energy for protons as a function of energy and the influence of interaction models on the average mean missing energy. $\log E$ is logarithm of energy, $\langle E_{miss} \rangle / E_{prim}$ is the average mean missing energy in a percentage of primary energy, max is maximum value of the average mean missing energy and min is minimum value of the average mean missing energy.

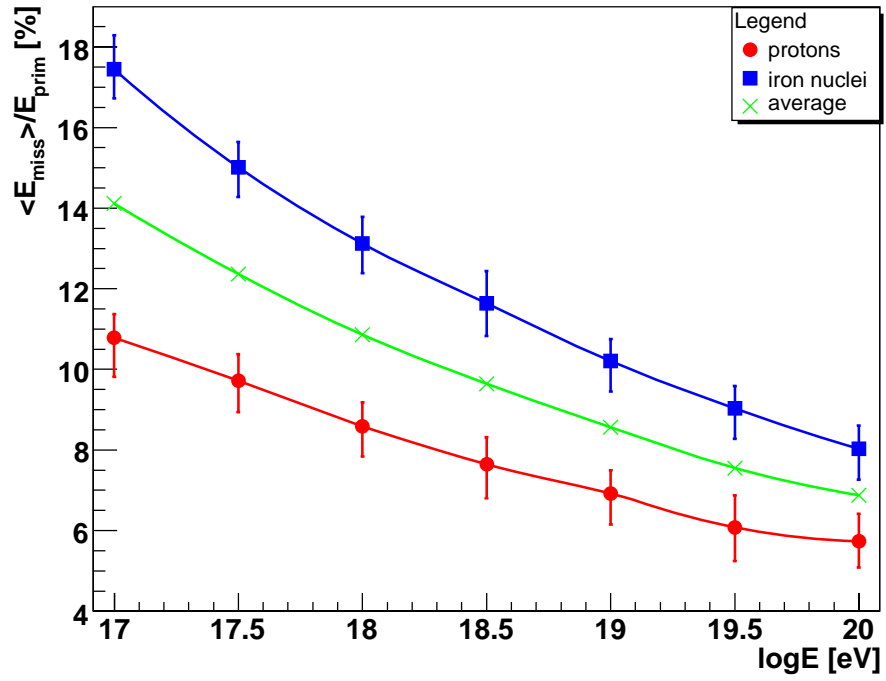


Figure 9.7: The average mean missing energy for protons and iron nuclei and the total average mean missing energy as a function of energy and the influence of the interaction models (error bars).

From the tables (9.2) and (9.3) and from the fig. (9.7) it can be clearly seen, that the average mean missing energy reaches the higher values for iron nuclei. The average mean missing energy for protons is smaller. Also it is clear, that with increasing energy the average mean missing energy is decreasing.

The influence of the interaction models in the case of iron nuclei as primary particles is mostly between 0.5 ~ 0.8 % and in the case that primary particles were protons, the influence of models is mostly between 0.6 ~ 1.0 %. It can be said, that the influence of the interaction models is almost constant with energy.

In the fig. (9.7) there is also the total average mean missing energy (plotted by a green line) calculated as average from all values of mean missing energy for both protons and iron nuclei. The values of the total average mean missing energy are also in the table (9.4).

Total $\langle E_{miss} \rangle / E_{prim}$	
$\log E$ [eV]	$\langle E_{miss} \rangle / E_{prim}$ [%]
17.0	14.1
17.5	12.4
18.0	10.9
18.5	9.6
19.0	8.6
19.5	7.6
20.0	6.9

Table 9.4: The total average values of the mean missing energy. $\log E$ is a logarithm of energy, $\langle E_{miss} \rangle / E_{prim}$ is the total average mean missing energy.

If some shower is measured by fluorescence technique, it cannot be exactly determined, which primary particle caused the shower of secondary particles. If this shower is reconstructed and the primary particle energy is to be determined, the missing energy has to be added. Table (9.4)) thus represents an optimal choice for the correction.

The error of this total average mean missing energy is given by the influence of the interaction models, by the distribution of the mean missing energy and also by the absence of the knowledge of the exact chemical composition of UHECR. Since RMS⁽²⁾ of missing energy distribution (see the figures (9.2)-(9.5) was found to be on the level of about 0.5% for iron primaries and about 1% in case of protons then it can be concluded from fig. (9.7) that the unknown chemical composition is the most significant contribution to error imposed to the process of energy determination from fluorescence detectors. Here we of course suppose that the fluorescence yield is known precisely enough which is still not true in reality.

²Root mean square.

Chapter 10

Summary and Conclusions

For purpose of this work SENECA and CONEX simulation codes were used together with following high energy interaction models: QGSJET01, QGSJETII, SYBILL, neXus and EPOS. In all cases GHEISHA 2002 was used as a low energy interaction model. The aim of this work was to determine the influence of high energy interaction models on the estimation of the chemical composition of CRs and on the missing energy.

SENECA simulation code together with high energy interaction models QGSJET01, QGSJETII, SYBILL and EPOS was used to simulate the maxima of showers (X_{max} - typical values are between $400 \sim 800 \text{ g/cm}^2$). The influence of the high energy interaction models on the $\langle X_{max} \rangle$ value was estimated. The typical influence of high energy interaction models is mostly between $8 \sim 12 \text{ g/cm}^2$. From the X_{max} values the estimation of the chemical composition of CRs was done (together with the data measured by the Pierre Auger Observatory). The two ways, how the chemical composition can be determined were used. The fraction of protons (which represents the lightest component of the CRs), the mean logarithmic mass and the influence of high energy interaction model on them were calculated. The influence of the high energy interaction model on the fraction of protons is mostly between $5 \sim 10 \%$ and on the mean logarithmic mass it is mostly between $0.2 \sim 0.4$ in $\langle \ln A \rangle$.

The results of the reconstruction of chemical composition of CRs are only model estimations supposing a given parametrization of Pierre Auger Observatory preliminary data. These results cannot be understood as an interpretation of the data measured by PAO. Nevertheless, they indicate, that at the highest energies the abundance of heaviest elements is increasing. This finding is in contrast with the last discoveries of the Pierre Auger Observatory. They found a correlation of the UHECR with the active galactic nuclei and this implies, that particles with such energies have to be light (due to the galactic magnetic field, in which trajectories of heavier particles are more curved). The disagreement of the results in this work with the last discoveries can be interpreted as the fact, that the parameters used in the high energy interaction models (multiplicity, cross sections, muon energy spectra, ...) are not estimated precisely enough.

The second goal of this work was to compute the missing energy. For this part of the work CONEX simulation code was used together with high energy interaction models

QGSJET01, QGSJETII, SYBILL and neXus. The estimates of the mean missing energy for different high energy interaction models were shown. The average mean missing energy over the models was estimated separately for protons and iron nuclei. The total mean missing energy was then calculated as average between the prediction for protons and iron nuclei, because protons are the lightest components of CRs and iron nuclei are the heaviest possible component of CRs. It can be supposed that the exact missing energy will be between them. The mean fraction of missing energy is decreasing with increasing energy. It was also shown, that the mean missing energy was higher in the case, when iron nucleus was the primary particle. It can be said, that the absence of knowledge of the exact composition of the cosmic rays at the highest energies is the most significant contribution to the total error of the determination of the missing energy. In all computations of the missing energy it is supposed, that the fluorescence yield is perfectly known.

Chapter 11

References

- [1] Sokolsky, P. (2004): Introduction to Ultrahigh Energy Cosmic Ray Physics, *Westview Press ISBN-10: 0813342120*.
- [2] Gaisser, T.K. (1990): Cosmic Rays and Particle Physics. *Cambridge University Press ISBN-10: 0521339316*.
- [3] Köhler, C. (1998): Entwicklung einer Methode zur Bestimmung der energie kosmischer TeV-Gamma-Quanten mit den Tscherenkow-Teleskopen der HEGRA-Kollaboration- Das Energiespektrum der aktiven Galaxie Mrk501. *Ph.D. Thesis, Ruprecht-Karls-universität Heidelberg*.
- [4] Šmída, R. (2002): Very high-energy astrophysics, *diploma thesis FMP Charles University Prague*.
- [5] Bhattacharjee, P.; Sigl, G. (1999): Origin and Propagation of Extremely High Energy Cosmic Ray. *astro-ph9811011*.
- [6] J. Abraham et al. (The Pierre Auger Collaboration)(2007): Correlation of the highest energy cosmic ray with nearby extragalactic objects. *Science 318, 938*.
- [7] Anchordoqui, L. for the Pierre Auger Collaboration (2007): Search for Coincidences in Time and Arrival Direction of Auger Data with Astrophysical Transients. *arXiv:0706.0989 [astro-ph]*.
- [8] Protheroe, R.J. (1998): Acceleration and Interaction of Ultra High Energy Cosmic Rays. *astro-ph/9812055*.
- [9] Hillas, A.M. (1984): The origin of ultra high energy cosmic rays. *Annual Review of Astronomy and Astrophysics, 22, 425*.
- [10] Gaisser, T.K. (2000): Origin of Cosmic Radiation. *arXiv:astro-ph/0011524v1*.
- [11] Unger, M.[The Pierre Auger Collaboration] (2007): Study of the Cosmic Ray Composition above 0.4 EeV using the Longitudinal Profiles of Showers observed at the Pierre Auger Observatory. *arXiv:0706.1495v1 [astro-ph]*.

- [12] Greisen, K. (1966): End to the Cosmic Ray Spectrum? *Physical Review letters*, 16, 748.
- [13] Zatsepin, G.T.; Kuzmin, V.A.(1966): Upper limit of the spectrum of cosmic rays. *Journal of Experimental and Theoretical Physics Letters*, 4, 78.
- [14] Nagano, M.; Watson, A.A. (2000): Observations and implications of the ultrahigh-energy cosmic rays. *Reviews of Modern Physics*, 72,689.
- [15] Cronin, J.W. (2004): The highest-energy cosmic rays. *arXiv:astro-ph:0402487v1*.
- [16] Trávníček, P. (2004): Detection of high-energy muons in cosmic ray showers. *Doctoral thesis FMP Charles University Prague*.
- [17] Janout, Z.; Kubašta, J.; Pospíšil, S. (1997): Úlohy z jaderné a subjaderné fyziky. *Vydavatelství ČVUT 1997*.
- [18] Heck, D.; Knapp, J.; Capdevielle, J.N.; Schatz, G.; Thouw, T.; (1998): CORSICA: A Monte Carlo Code to Simulate Extensive Air Showers. *Forschungszentrum Karlsruhe GmbH, Karlsruhe 1998. FZKA 6019*.
- [19] Boháčová, M. (2006): Pierre Auger fluorescence detector study of the air fluorescence. *Doctoral thesis FMP Charles University Prague*.
- [20] Reece, R.D. et al. (2005): Air Fluorescence Photon Yield In Cosmic Ray Showers. http://reu.physics.ucla.edu/common/papers/2005/ryan_reece.pdf.
- [21] Gaisser, T.K.; Hillas, A.M. (1977): Proc. 15th ICRC.
- [22] Kamata, K.; Nishimura, J. (1958): *Prog. Theoretical Phys.*, Suppl.6,pp.93-100.
- [23] Drescher, H.; Glennys, R. F. (2003): Air Shower Simulations in a Hybrid Approach using Cascade Equations. *Phys. Rev.*, D67:116001,2003.
- [24] Werner, K. (1993): Strings, pomerons, and the venus model of hadronic interactions at ultrarelativistic energies.*Phys. Rep.* 232 87.
- [25] Kalmykov, N.N.; Ostapchenko, S.S.; Pavlov, A.I.; (1997): Quark-Gluon String Model AND Eas Simulation Problems at Ultra-High Energies. *Nucl. Phys. Proc. Suppl.* 52B, 17.
- [26] Ranft, J.; Engel, R. (1995): Hadronic photon-photon interactions at high-energies.*Phys. Rev.* D51 64.
- [27] Fletcher, R.S.; Gaisser, T.K.; Lipari, P.; Stanev, T. (1994): SIBYLL: An Event generator for simulation of high-energy cosmic ray cascades. *Phys. Rev.* D50 5710.
- [28] Werner, K. et al., (2006):Parton Ladder Splitting and the Rapidity Dependence of Transverse Momentum Spectra in Deuteron-Gold Collisions at RHIC. *Phys. Rev.* C74 044902 and *hep-ph/0506232*.

- [29] Drescher, H.J. et al., (2000): Parton-Based Gribov-Regge Theory. *Phys. Rep.* 333, 329, *hep-ph/0007198*.
- [30] Fesefeldt, H. (1985): The simulation of hadronic showers. *PITHA 85/02, Aachen*.
- [31] Sorge, H. et al., (1989): *Nucl. Phys. A* 498, 567-576;
 Battistoni, G. et al., (2004): *Braz. J. Phys.* 34, 897-900;
 Andersen, V. et al., (2004): *Adv. Space Res.* 34, 1302-1310.
- [32] Unger, M. (2006): Shower Profile Reconstruction from Fluorescence and Cherenkov light. *GAP-2006-010*.
- [33] Groom, D.E. et al. (2000): Review of Particle Physics. *The European Physical Journal C* 15 (2000) 1.
- [34] Bossard, G. et al. (2001): Cosmic Ray Air Shower Characteristics in the Framework of the Parton-based Gribov-Regge Model NEXUS. *Phys. Rev.*, D63:054030, 2001.
- [35] Kalmykov, N.N. (2007): One-dimensional Hybrid Approach to Extensive Air Shower Simulation. *arXiv:astro-ph/0606564v1*.
- [36] T. Pierog et al. *Nucl. Phys. B (Proc. Sup)* 151 (2006) Proceedings of 13th International Symposium on Very High-Energy Cosmic Ray Interactions at the NESTOR Institute, Pylos, Greece, 6-12 Sep 2004. e-print Archive: *astro-ph/0411260*.
- [37] SENECA Usersguide Version 1.3.2, Hans-Joachim Drescher, 17.10.2006.
- [38] Heck, D. (2005): The Influence of Hadronic Interaction Models on Simulated Air-Showers: A Phenomenological Comparison. *talk presented at the VIHOS CORSIKA School, Lauterbad*.

Other sources

[39] The official web pages of the Pierre Auger Observatory:

<http://www.auger.org>

[40] The Czech group web pages of the Pierre Auger observatory:

<http://www-hep2.fzu.cz/Auger/cz/>

[41] The web pages of the ROOT:

<http://root.cern.ch/>

[42] <http://www.mpi-hd.mpg.de/hfm/HESS/>

[43] http://en.wikipedia.org/wiki/Neutron_star

[44] <http://imagine.gsfc.nasa.gov/docs/science/known11/bursts.html>

[45] http://en.wikipedia.org/wiki/Supernova_remnant

[46] http://imagine.gsfc.nasa.gov/docs/science/known12/supernova_remnants.html

[47] <http://www.telescopearray.org/outreach/intro.html#discovery>

[48] <http://helios.gsfc.nasa.gov/history.html>